AGU PUBLICATIONS

JGR

Journal of Geophysical Research: Oceans

RESEARCH ARTICLE

10.1002/2015JC011284

Key Points:
- Analytical model is derived to describe waves in tropical cyclones
- Compared to altimeter measurements, the model demonstrates convincing agreement
- Criterion for generation of trapped abnormal waves by moving extreme events is suggested

Correspondence to:
V. Kudryavtsev,
kudr@rshu.ru

Citation:
Kudryavtsev, V., P. Golubkin, and B. Chapron (2015), A simplified wave enhancement criterion for moving extreme events, *J. Geophys. Res. Oceans*, *120*, 7538–7558, doi:10.1002/2015JC011284.

Received 31 AUG 2015
Accepted 22 OCT 2015
Accepted article online 30 OCT 2015
Published online 20 NOV 2015

A simplified wave enhancement criterion for moving extreme events

Vladimir Kudryavtsev[1,2], Pavel Golubkin[1], and Bertrand Chapron[1,3]

[1]Satellite Oceanography Laboratory, Russian State Hydrometeorological University, St. Petersburg, Russia, [2]Remote Sensing Department, Marine Hydrophysical Institute, Sebastopol, Russia, [3]Laboratoire d'Oceanographie Spatiale, Ifremer, Brest, France

Abstract An analytical model is derived to efficiently describe the wave energy distribution along the main transects of a moving extreme weather event. The model essentially builds on a generalization of the self-similar wave growth model and the assumption of a strongly dominant single spectral mode in a given quadrant of the storm. The criterion to anticipate wave enhancement with the generation of trapped abnormal waves defined as $gr/u_r^2 \approx c_T(u_r/V)^{1/q}$, with r, u, and V, radial distance, average sustained wind speed, and translation velocity, respectively. Constants q and c_T follow the fetch-law definitions. If forced during a sufficient time scale interval, also defined from this generalized self-similar wave growth model, waves can be trapped and large amplification of the wave energy will occur in the front-right storm quadrant. Remarkably, the group velocity and corresponding wavelength of outrunning wave systems will become wind speed independent and solely related to the translating velocity. The resulting significant wave height also only weakly depends on wind speed, and more strongly on the translation velocity. Compared to altimeter satellite measurements, the proposed analytical solutions for the wave energy distribution demonstrate convincing agreement. As analytically developed, the wave enhancement criterion can provide a rapid evaluation to document the general characteristics of each storm, especially the expected wavefield asymmetry.

1. Introduction

Owing to satellite-based observations, extreme sea states related to severe weather events, especially tropical cyclones (TC), can more commonly be reported, directly analyzed [e.g., *Quilfen et al*., 2010, 2011; *Hanafin et al*., 2012] or indirectly characterized from short and long distance radiated swell fields [e.g., *Holt and Gonzalez*, 1986; *Holt et al*., 1998; *Collard et al*., 2009; *Delpey et al*., 2010]. These measurements can be critical for short-term forecasting, but also offer means to better examine the role of extremes on ocean circulation and ocean heat transport.

Capable of generating severe wave conditions, intense weather events are generally relatively small low-pressure systems, moving rapidly. Mainly due to translation characteristics, surface waves in the TC right sector can remain under high wind forcing conditions for longer periods than usual [*Cline*, 1920; *Tannehill*, 1936]. This has been termed extended fetch, trapped fetch, or group velocity quasi resonance [e.g., *King and Shemdin*, 1978; *Dysthe and Harbitz*, 1987; *Young*, 1988a; *Bowyer and MacAfee*, 2005; *Young and Vinoth*, 2013]. A TC wavefield is thus likely more asymmetrical than the corresponding wind field: wind waves in the TC right sector are more developed with larger heights than waves in the left one. Such sea state conditions can impact momentum fluxes [*Holthuijsen et al*., 2012] and influence the TC intensification [e.g., *Moon et al*., 2008]. Also, this can possibly enhance more asymmetrical intense mixing and upwelling to entrain thermocline water into the mixed layer, leaving behind a cooler asymmetrical wake of SST, increasingly depressed for relatively slow moving TCs [e.g., *Reul et al*., 2014, Figure 4], and several degrees larger on the right-hand side of the TC track. As also reported, this can further be accompanied by the sea surface salinity (SSS) marked changes [*McPhaden et al*., 2009; *Grodsky et al*., 2012; *Reul et al*., 2014], to possibly further affect the event's intensification [*Balaguru et al*., 2012].

Asymmetrical wind and wavefields can further strongly modulate whitecap properties, coverage, and thickness [e.g., *Reul and Chapron*, 2003]. Oceanic whitecaps also mark areas with actively producing sea spray

droplets via bubble bursting (film and jet droplets), and via the wind tearing off wave crests (spume droplets). These combined effects possibly yield additional radio brightness [*Raizer*, 2007] to impact passive microwave radiometer measurements to infer surface extreme wind speeds [*Uhlhorn and Black*, 2003; *Reul et al*., 2012].

Moon et al. [2003] performed a comprehensive investigation of wind wavefield generated by TC Bonnie using WAVEWATCH III model [*Tolman*, 2009], buoy and airborne Scanning Radar Altimeter (SRA) measurements. Results confirmed the essential role of nonlinear wave-wave interactions to continually shape and stabilize the spectrum to a standard JONSWAP-like evolution. Close to the TC centers, *Ochi* [1993] and *Young* [1998] already reported data showing strong similarities with typical fetch-limited observations. Except for the TC right-rear quadrant with respect to its forward direction, *Hu and Chen* [2011] also reported that most of measured buoy spectra are monomodal, similar to those under fetch-limited and unidirectional wind conditions. *Moon et al*. [2003] further indicate that the translation of a wind system tends to straighten out the effect of the wind field curvature. Especially in the right sector, waves can thus remain aligned with the wind for longer time. In such conditions, the existence of a single spectral mode in a given quadrant simplifies the wave growth conditions to near idealized.

To efficiently simulate waves under TC, a key issue remains is to define an equivalent or effective fetch. As suggested [*Young*, 1988b], the equivalent fetch can be defined in terms of the hurricane parameters: translation velocity and maximum wind speed, radius of maximum wind [see, e.g., *Young*, 2003, relation (5)–(7)]. *Bowyer and MacAfee* [2005], following *Dysthe and Harbitz* [1987], suggested a Lagrangian approach to simulate trajectory of growing waves in an idealized moving storm. The numerical experiments showed that, within the wave containment (front-right) quadrant, wave height enhancement can be positive or negative depending on the degree of synchronicity between the TC motion and the acceleration of the generated waves. *Bowyer and MacAfee* [2005] parameterized their results to provide simple empirical relations to identify possible abnormal wave enhancement for practical (advance warning) applications.

In this paper, our motivation is to further dwell on the self-similarity aspect of wind wave growth and to suggest a simplified analytical model to efficiently evaluate the wave energy distribution. Applied to a wide range of conditions (wind speed, TC translation velocity, and radius of maximum wind speed), derived analytical solutions are robust unique functions of a critical nondimensional fetch, essentially governed by the ratio between the translating velocity and the wind speed. This derivation is not intended to compete with even the crudest numerical wind wave generation model. Yet as analytically developed, a direct evaluation can be simply performed using the proposed formulation. This helps to rapidly anticipate and document the role of partial resonance effects to increase the effective fetch and duration of the wave-growth process in the direction of the TC motion, i.e., the wave trapping phenomenon.

For our purpose, satellite altimeter measurements, together with estimates of TC characteristics, are used to assess the proposed formulations and the simplified wave enhancement criterion for moving extreme events.

2. Data and Methods

2.1. Altimeter Data Set

Altimeter data from four missions are used in this study, namely, Jason-1, Jason-2, CryoSat-2, and SARAL/AltiKa. Jason-1 satellite, a follow-on to the TOPEX/Poseidon mission, was launched in December 2001 and had been operated until July 2013. Its main instrument, Poseidon-2, is a nadir-looking dual-frequency radar altimeter operating in Ku-band (13.575 GHz) and auxiliary C-band (5.3 GHz). The data used here are Geophysical Data Records (GDRs) obtained from the Physical Oceanography Distributed Active Archive Center (PODAAC; http://podaac.jpl.nasa.gov/) of National Aeronautics and Space Administration (NASA) Jet Propulsion Laboratory (JPL).

Ocean Surface Topography Mission (OSTM) Jason-2 satellite was launched in June 2008 with Poseidon-3 altimeter on board. Characteristics are essentially the same as of its predecessor, with two additional experimental operational modes to improve data acquisition in coastal areas and continental waters. GDRs were provided by National Oceanographic Data Center (NODC; http://www.nodc.noaa.gov/) operated by the National Oceanic and Atmospheric Administration (NOAA).

Table 1. TCs Parameters and Altimeter Crossing Time

TC	Closest Report Date and Time (UTC)	TC Center Position	Altimeter Time (UTC)	r34, nm (NE/SE/SW/NW)	r50, nm (NE/SE/SW/NW)	r64, nm (NE/SE/SW/NW)	R_m (nm)	U_m (kn)	V_{tr} (m s^{-1})	P_c (hPa)	P_n (hPa)
Malakas	24 Sep 2010 0600	26.3°N, 141.3°E	03:36:48	155/155/130/145	75/75/55/65	30/30/25/30	20	90	10.1	956	1001
Songda	27 May 2011 0000	18.2°N, 123.9°E	02:35:02	165/165/160/150	75/75/70/70	45/45/45/45	15	140	5.7	918	1002
Ma-on	17 Jul 2011 0000	23.5°N, 135.6°E	02:01:12	190/180/180/190	100/85/85/100	50/50/50/50	20	110	6.6	941	998
Muifa	6 Aug 2011 1200	29.4°N, 124.9°E	12:19:03	210/180/160/190	125/115/70/110		25	65	3.7	974	996
Talim	19 Jun 2012 0600	20.2°N, 115.7°E	06:22:32	100/120/120/100			45	45	4.6	996	989
Trami	20 Aug 2013 0300	22.6°N, 128.2°E	03:47:05	80/75/65/75	30/30/30/30		25	55	8.1	982	995
Bolaven	24 Aug 2012 0600	21.7°N, 133.3°E	05:07:00	180/180/160/160	100/60/60/80	20/20/20/20	20	110	3.5	940	995
Jelawat	28 Sep 2012 0600	23.4°N, 124.5°E	08:53:22	165/165/155/155	120/120/110/110	70/70/70/70	20	115	5.0	937	1004
Prapiroon	16 Oct 2012 1800	22.8°N, 128.6°E	18:29:56	160/165/165/160			30	45	3.8	989	1005
Bopha	3 Dec 2012 1200	7.4°N, 128.9°E	09:21:02	115/105/100/110	65/55/50/65	35/30/30/35	5	140	7.9	918	1008
Soulik	8 Jul 2013 1800	19.5°N, 141.5°E	20:24:12	90/80/70/85	35/30/30/30		25	70	5.4	970	1006
Soulik	11 Jul 2013 0000	21.1°N, 135.9°E	21:06:39	170/155/150/170	85/75/75/85	55/45/45/55	17	105	6.2	944	1003
Utor	11 Aug 2013 0000	14.5°N, 125.9°E	21:30:08	115/100/100/115	55/50/50/55	35/35/35/35	15	95	5.6	952	1005
Usagi	18 Sep 2013 1800	17.1°N, 128.7°E	19:06:26	85/85/85/85	40/40/40/40	20/20/20/20	20	90	1.4	956	1002
Usagi	21 Sep 2013 0000	20.6°N, 121.7°E	21:43:48	175/155/180/185	110/100/105/100	60/60/60/60	12	120	4.5	933	1000
Fitow	3 Oct 2013 0600	20.6°N, 129.7°E	05:17:30	160/150/135/135	75/75/65/60		30	70	2.6	970	1005
Wipha	14 Oct 2013 1800	25.6°N, 133.9°E	16:06:08	230/205/200/210	135/115/95/125	65/65/55/55	25	100	7.4	948	1004
Wipha	15 Oct 2013 1200	30.4°N, 136.4°E	09:09:32	220/205/175/195	125/115/95/115	50/50/45/45	30	70	13.1	970	1002
Haiyan	8 Nov 2013 0000	11.0°N, 124.7°E	21:32:35	130/115/120/130	65/60/60/70	50/45/40/50	15	165	11.3	899	1000
Isabel	14 Sep 2003 0000	22.9°N, 63.3°W	23:55:53					135	6.1	935	
Julia	18 Sep 2010 0600	26.9°N, 49.8°W	04:02:01	150/135/75/105	80/60/30/40			55	8.4	991	

Synthetic aperture radar (SAR)/Interferometric Radar Altimeter (SIRAL) onboard CryoSat-2 satellite was launched in April 2010. We use the "low-resolution mode" when the instrument operates as a conventional Ku-band (13.575 GHz). The data are available at the European Space Agency (ESA) Earth Online website (https://earth.esa.int/).

SARAL/AltiKa launched in February 2013 is the first satellite altimeter operating in Ka-band (35.75 GHz). This higher frequency leads to an improved spatial and height resolution. Ka-band is more sensitive to precipitation; therefore, data from TC rainbands were often lost. GDRs are distributed through the Archiving, Validation and Interpretation of Satellite Oceanographic data (AVISO) portal (http://www.aviso.altimetry.fr/).

2.2. TC Data Set

As selected, the altimeter data set consists of Jason-1 pass of Atlantic TC Isabel (2003), previously thoroughly analyzed by *Quilfen et al*. [2006], Jason-1 pass of Atlantic TC Julia (2010), and number of different altimeter passes crossing TCs (typhoons) in the western North Pacific. TCs positions with 6 h time interval were taken from the Joint Typhoon Warning Center (JTWC) best-track data for 2010–2013 (for typhoons) and NOAA HURDAT (for hurricanes). Position of a TC's eye relative to the altimeter crossing point was derived using linear interpolation between two successive TC positions. The mean TC translation velocity, V, is estimated from the distance between two successive positions divided by 6 h interval. As selected, altimeter passes cross the front-right quadrant at a distance less than $10R_m$, with R_m the radius of maximum wind speed.

In total, 21 altimeter passes have been selected, listed in Table 1 with auxiliary data taken from JTWC best-track data (for typhoons) and NOAA HURDAT (for hurricanes): maximum wind speed, U_m, radius of maximum wind, R_m, radii of 34, 50, and 64 kt winds ($r34$, $r50$, and $r64$) for each of the quadrants (northeast, southeast, southwest, and northwest), central, P_c, and ambient, P_n, pressure, as well as time of the crossing point of TC trajectory by altimeter track.

Among these cases, we further selected cases with altimeter tracks crossing a TC from front-right to rear-left quadrant (or vice versa) at the distance less than R_m from the eye, namely, two tracks crossing hurricanes Isabel and Julia, and three tracks crossing typhoons Songda, Muifa, and Prapiroon. Trajectories of these typhoons and the corresponding altimeter ground tracks are shown in Figure 1. Trajectories of the Atlantic hurricanes and corresponding altimeter ground tracks can be found in *Quilfen et al*. [2006] for TC Isabel and in Figure 12 for TC Julia. The altimeter tracks overlaid on the IR images of the TCs are shown in

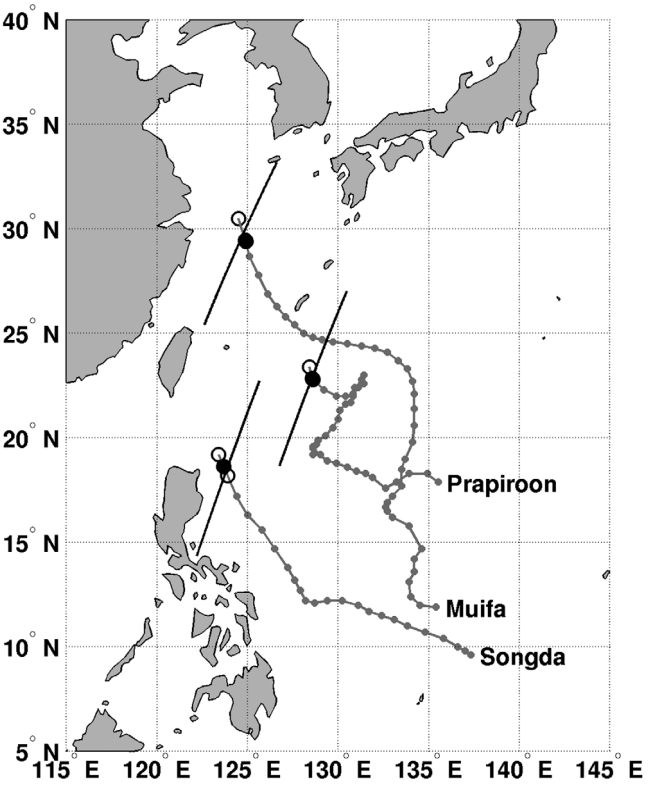

Figure 1. Typhoons Songda, Muifa, and Prapiroon best tracks as determined by JTWC, and altimeter passes crossing these typhoons. Open circles indicate TCs locations before and after altimeter crossing time of the corresponding track, and black dots indicate interpolated TC location at the crossing time, small gray circles indicate 6-hourly TC positions.

Figure 2, to confirm crossings within the TC inner cores. Enhancement of the wave energy in the right-front sector is evident for all TC cases.

2.3. Wind Field

While certainly limited by their relatively coarse across-track sampling, altimeter measurements have been demonstrated to provide very valuable wind speed information [e.g., *Young*, 1993; *Quilfen et al*., 2006, 2011]. In particular, thanks to their dual-frequency capability, altimeter signals can be analyzed to jointly estimate surface wind speed and significant wave height, along with the rain rate in extreme weather events [*Quilfen et al*., 2010]. Among the considered cases, this method only applies to Jason-1 and Jason-2 measurements, altimeters with dual-frequency capabilities. The derived wind speed profiles along the altimeter tracks crossing selected TCs are shown in Figures 4–7 and 13.

In this study, the parametric model suggested by *Holland* [1980] is also used. For each of the quadrants of a given TC, gradient wind speed at the radius r from TC center was reconstructed using parameters listed in Table 1, as:

$$U=\left[\frac{AB(P_n-P_c)\exp\left(-A/r^B\right)}{\rho r^B}+\frac{r^2f^2}{4}\right]^{1/2}-\frac{rf}{2}, \quad (1)$$

where f is the Coriolis parameter, ρ is air density (taken as 1.15 kg m^{-3}), and A and B are the scaling parameters defining the shape of the wind profile. Wind speed at standard 10 m reference level is derived from the gradient wind speed with adjusted multiplying factor 0.86–0.89 [*Franklin et al*., 2003]. Expression (1) was fitted to the best-track data values of U_m, R_m, $r34$, $r50$, and $r64$. Parameters A and B were chosen to minimize the difference between the wind profile model and the best-track wind speed values. As such, the factor applied to the gradient wind is absorbed in the tuning parameters. This procedure is applied to each of the TC quadrants, and 2-D wind fields are reconstructed from truncated Fourier series. In two cases, TCs Muifa and Prapiroon, R_m derived from altimeter wind speed largely deviates from reported by JTWC (Table 1). In these cases, the model (1) was fitted to altimeter measurements, and further used in the model simulations.

In the absence of more detailed wind data for typhoons, reconstructed wind fields are used for further analysis. Figure 3 shows reconstructed 10 m wind field for TCs Songda, Muifa, and Prapiroon, and H*WIND analysis for TC Isabel, when altimeter tracks were close to the TC eye—at the distance less than R_m. Proximity of altimeter tracks to the TC eye is confirmed by the corresponding altimeter wind speed profiles (Figures 4–7), where local minima of wind speed are well detected in each of the cases.

2.4. Wave Energy Observations

Profiles of the wave energy, $e=H_s^2/16$, along the altimeter tracks crossing TCs almost through their eyes (at the distance less than R_m), from the front-right to rear-left quadrants (or vice versa) are shown in Figures 4–7. As anticipated, a significant asymmetry is systematically revealed in the wave energy profiles—the

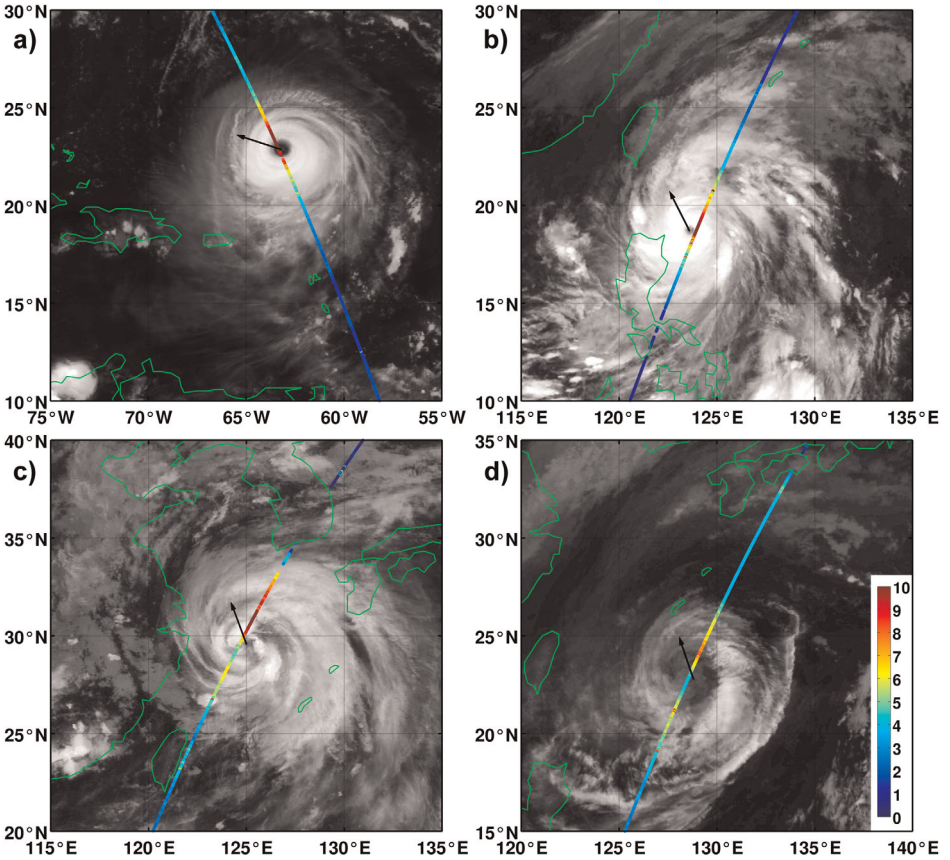

Figure 2. Altimeter tracks (color lines) overlaid on IR images of TCs: (a) Isabel, (b) Songda, (c) Muifa, and (d) Prapiroon. Black arrows attached to TC eyes indicate direction of the TC movement. Color bar shows values of significant wave heights along the altimeter tracks. IR images: for TC Isabel, GOES-12 20030913 2345 UTC, from NOAA Comprehensive Large Array-data Stewardship System (CLASS; http://www.class.ncdc.noaa.gov/); for TCs Songda, Muifa, and Prapiroon, MTSAT-2 gridded data from Center for Environmental Remote Sensing, Chiba University (http://www.cr.chiba-u.jp/), 20110806 1230 UTC (Muifa), 20121016 1832 UTC (Prapiroon), and 20110527 0232 UTC (Songda).

energy in the front-right quadrant markedly exceeds the energy in the rear-left one. Wind profiles corresponding to the H*WIND analysis for TC Isabel (Figure 4), the model (1) for TC Songda (Figure 5), and derived from altimeter measurements are symmetrical relative to TC eye. The observed asymmetry in the wave energy thus likely indicates wave trapping effects. For Prapiroon (Figure 6) and Muifa (Figure 7), altimeter-derived winds exhibit large asymmetries between front-right and rear-left quadrants. For these cases, observed asymmetry in wave energy is presumably caused by a combination of wave trapping and wind asymmetry.

The data listed in Table 1 are all used to infer the effective fetch for the waves in the wave-containment front-right quadrant of TC. According to the self-similarity concept [*Kitaigorodskii*, 1962], the dimensionless wave energy, $\tilde{e}=eg^2/u^4$, and the spectral peak frequency, $\tilde{\omega}_p=\omega_p u/g$, are universal functions of the dimensionless fetch, $\tilde{x}=xg/u^2$, usually expressed as power laws:

$$\tilde{\omega}_p \equiv \alpha = c_\alpha \tilde{x}^q, \tag{2a}$$

$$\tilde{e} = c_e \tilde{x}^p, \tag{2b}$$

where u is wind speed at 10 m height, g is the gravity acceleration, $\alpha=u/c_p$ is inverse wave-age, c_p is phase velocity of the spectral peak, c_e, p, and c_α, q are "constants." Using (2), the dimensionless energy can be represented as a function of the wave age only:

$$\tilde{e} = c_e c_\alpha^{-p/q} \alpha^{p/q}. \tag{3}$$

Based on weakly turbulent scaling arguments, recent studies [*Badulin et al.*, 2007; *Gagnaire-Renou et al.*, 2011; *Zakharov et al.*, 2015] also predict fetch laws in the form similar to (2). However, parameters of these

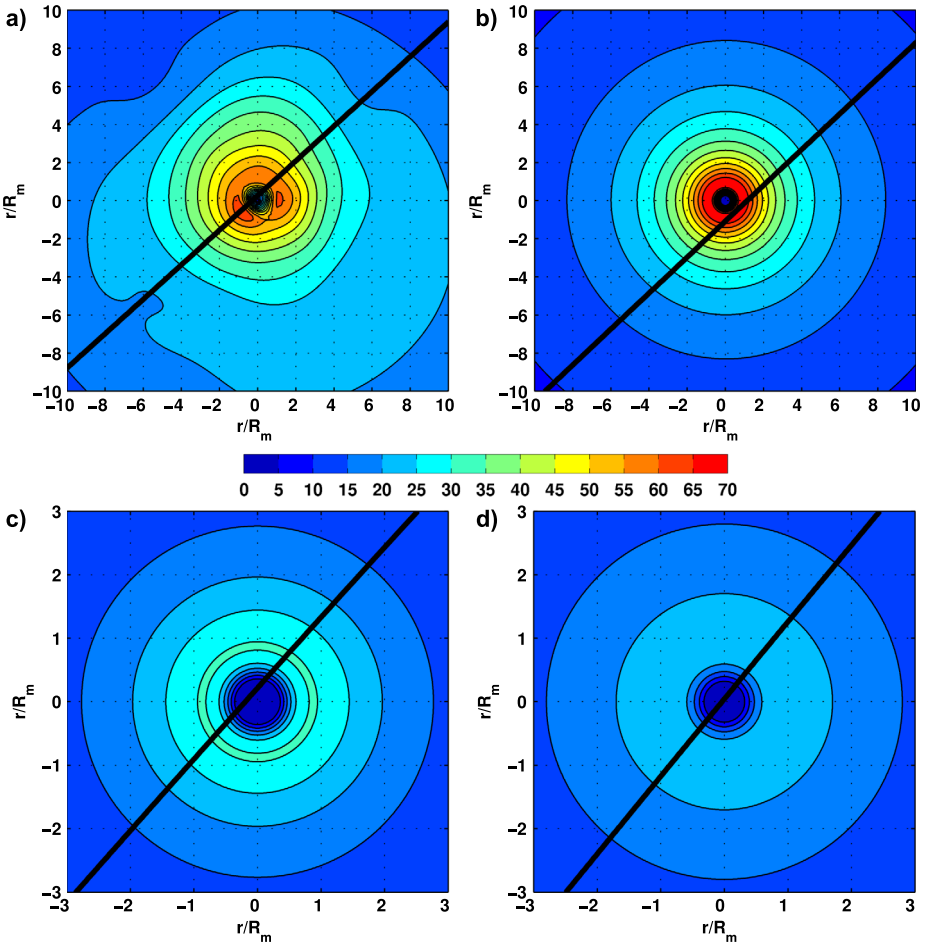

Figure 3. Wind field for TC (a) Isabel, (b) Songda, (c) Muifa, and (d) Prapiroon. Figure 3a is H*WIND field produced by NOAA Hurricane Research Division; Figures 3b–3d are model wind field reconstructed using (1) with parameters listed in Table 1. Black solid lines indicate the altimeter ground tracks. Direction of TC movement for each of the cases is upward. Radii to maximum wind, R_m, used for scaling are: (a) R_m = 30 km, (b) R_m = 28 km, (c) R_m = 176 km, and (d) R_m = 145 km.

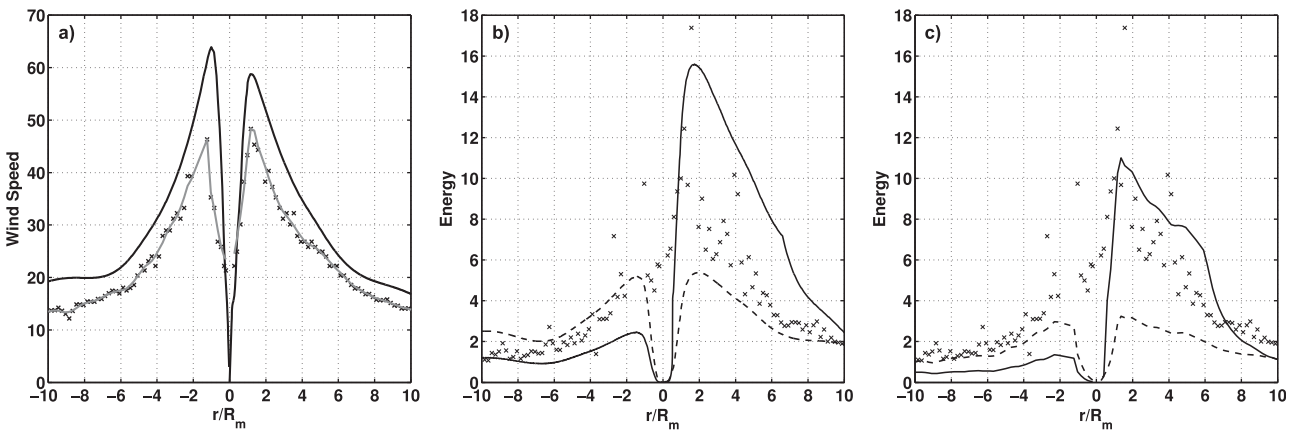

Figure 4. TC Isabel. (a) Transect of the H*WIND field along the altimeter track (solid line), wind speed measured by the altimeter (symbols), and smoothed altimeter wind speed (gray line). (b) Wave energy measured by the altimeter (symbols), the model wave energy profile calculated on (6) and (9) using H*WIND (solid line), and the reference (if TC is stationary) energy profile corresponding to H*WIND profile (dashed line). (c) Wave energy measured by the altimeter (symbols), the model wave energy profile calculated on (6) and (9) using altimeter wind speed (solid line), and the reference (if TC is stationary) energy profile corresponding to the altimeter wind speed (dashed line). Radius to maximum wind, R_m, used for scaling is R_m = 30 km.

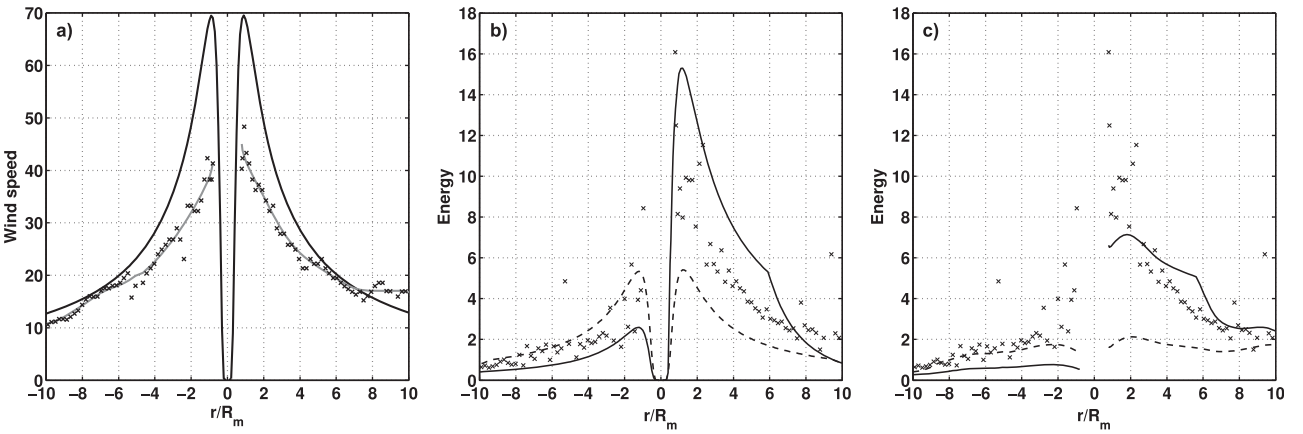

Figure 5. TC Songda. (a) Transect of the model, equation (1), wind field along the line parallel to the altimeter track and crossing the eye (solid line), wind speed measured by the altimeter (symbols), and smoothed altimeter wind speed (gray line). (b) Wave energy measured by the altimeter (symbols), the model wave energy profile calculated on (6) and (9) using the model (1) wind speed (solid line), and the reference (if TC is stationary) energy profile corresponding to the model wind speed (dashed line). (c) Wave energy measured by the altimeter (symbols), the model wave energy profile calculated on (6) and (9) using altimeter wind speed (solid line), and the reference (if TC is stationary) energy profile corresponding to the altimeter wind speed (dashed line). Radius to maximum wind, R_m, used for scaling is $R_m = 28$ km.

laws are not constants but shall depend on the stage of wave-development (see brief overview in Appendix A). In the present study, following *Badulin et al.* [2007], as the reference empirical fetch law, we adopt parameterizations suggested by *Babanin and Soloviev* [1998].

The effective fetch, x_{ef}, is defined as $x_{ef} = (u_{obs}^2/g)(\tilde{e}_{obs}/c_e)^{1/p}$, where u_{obs} and $\tilde{e}_{obs}$ are observed wind speed and wave energy. Effective fetches are deduced from the significant wave height recorded along the altimeter tracks listed in Table 1. Altimeter measurements are averaged around the maximum. These averaged values together with local wind speed, u, and local radius, r, are then used to retrieve the effective fetch, reported in Figure 8 as a function of the ratio between TC translation speed V and wind speed u. TC radii where the altimeter wave heights were observed are ranged from 10 to 150 km; this range overlaps typical radii of the maximum wind speed as reported by *MacAfee and Bowyer* [2005]. For comparison, the effective fetch proposed by *Young and Vinoth* [2013], calculated for TC radius $r = 100$ km and wind speeds 30 and 50 m/s, is also shown, in good agreement with the data for $0.1 \leq V/u \leq 0.2$. As indicative, the data shown in Figure 8 are fitted by

$$x_{ef}/r = 1.4 \times \exp(5.3V/u). \quad (4)$$

As inferred, the effective fetch for a stationary TC, i.e., $V \approx 0$, tends to $x_{ef} \approx 1.4r$. Notice that empirical relationship (4) does not pretend on a universality; it is rather shown here to illustrate that, on one hand, the

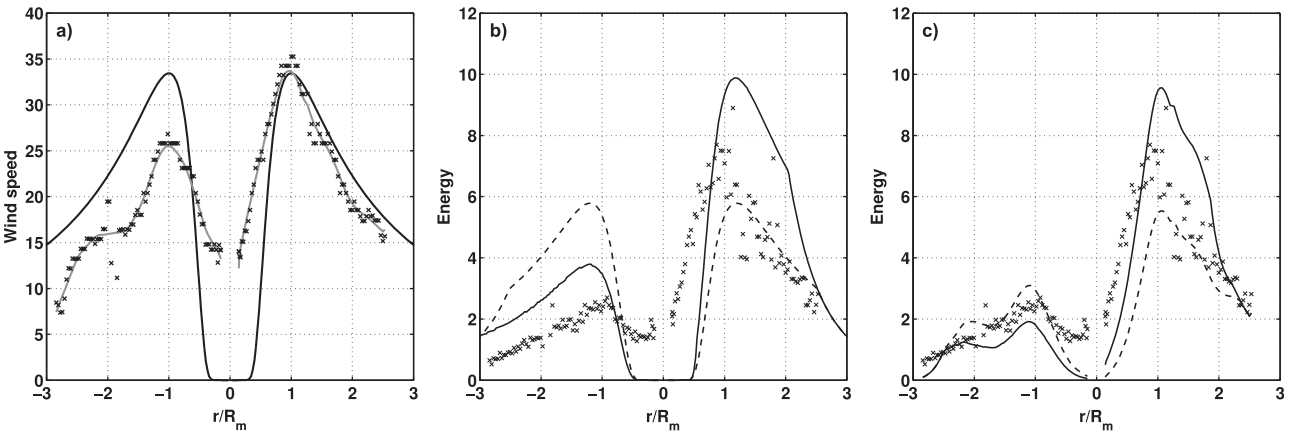

Figure 6. Same as in Figure 5 but for TC Muifa, $R_m = 176$ km.

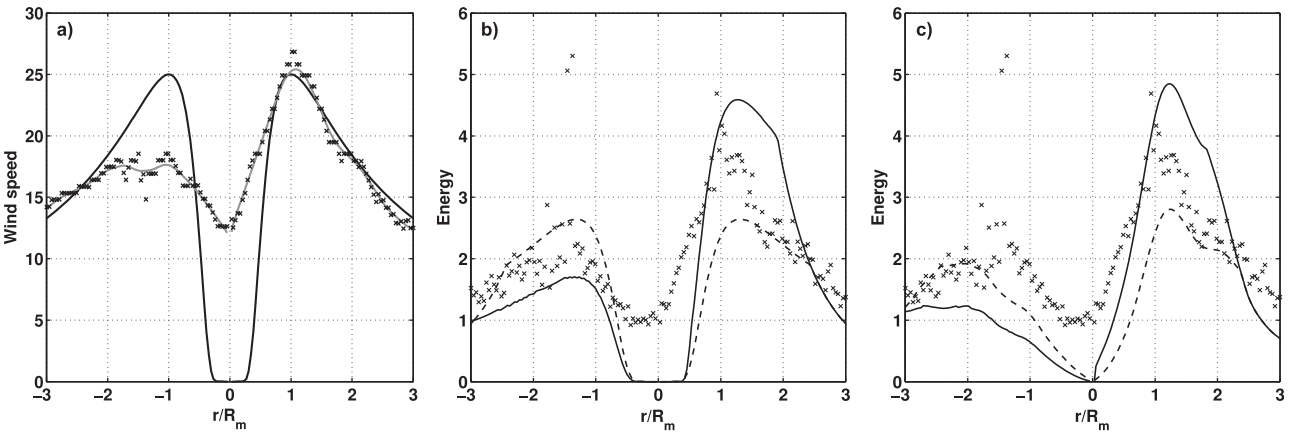

Figure 7. Same as in Figure 5 but for TC Prapiroon, $R_m = 145$ km.

effective fetch is dependent on TC translation speed, and, on the other hand, is proportional to TC radius. In section 3.3 (see also Figure 11), we justify that the "true" ratio x_{ef}/r is a universal function of the ratio between TC radius and the critical fetch (5) that is not simply proportional to V/u.

The reference wave energy profiles defined for stationary TC, equation (2b) with $x = 1.4r$, are shown in Figures 4–7. These reference profiles thus take into account the TC structure asymmetry (wind speed and radius). Deviation of measured energy from this reference estimate should then relate to the effect of the wave trapping. For TCs Isabel and Songda (Figures 4 and 5), the reference calculations severely underestimate the altimeter-derived wave energy in the wave-containment (front-right) sector. For TCs Muifa and Prapiroon (Figures 6 and 7), the measured wave energy follows, in general, the reference one calculated using altimeter wind speed, suggesting that observed asymmetry in significant wave heights is likely imposed by the wind asymmetry, as captured from the altimeter estimates. The model wind speed is symmetrical, and observed difference between the front-right and rear-left sectors could only be attributed to wave trapping effects. Note that the highest waves are underestimated for both wind profiles; therefore, the wave trapping mechanism can also be invoked to explain the observed wave asymmetry in TCs Muifa and Prapiroon.

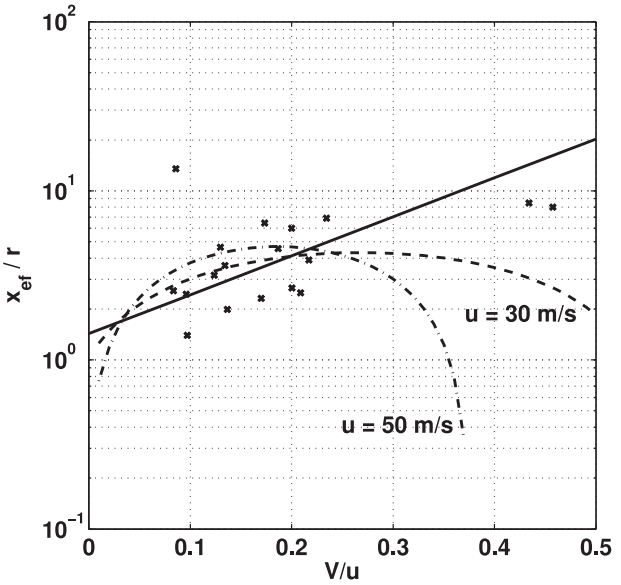

Figure 8. Symbols: effective fetch for local maxima of wave energy scaled by radius of their location against the ratio of TC translation velocity to the local wind speed. Solid line: best fit of the data, $x_{ef}/r = 1.4\exp(5.3V/u)$. Dashed lines: parameterization by *Young and Vinoth* [2013] for $u = 30$ m/s and $u = 50$ m/s at $r = 100$ km.

3. A Simplified Model Formulation

3.1. Approach

A generalization of the self-similar wave growth model (2) and (3) for a moving storm is presented in Appendix A. We sketch an idealized TC wind field as presented in Figure 9. We first analyze distribution of the wave energy along the transect A-B where wave energy asymmetry is expected, namely, wave enhancement along O-A due to the wave trapping effect, and abatement along O-B due to a reduced duration of wave generation under winds opposing the TC translation direction.

To derive analytical solutions, we assume that wind waves develop along straight

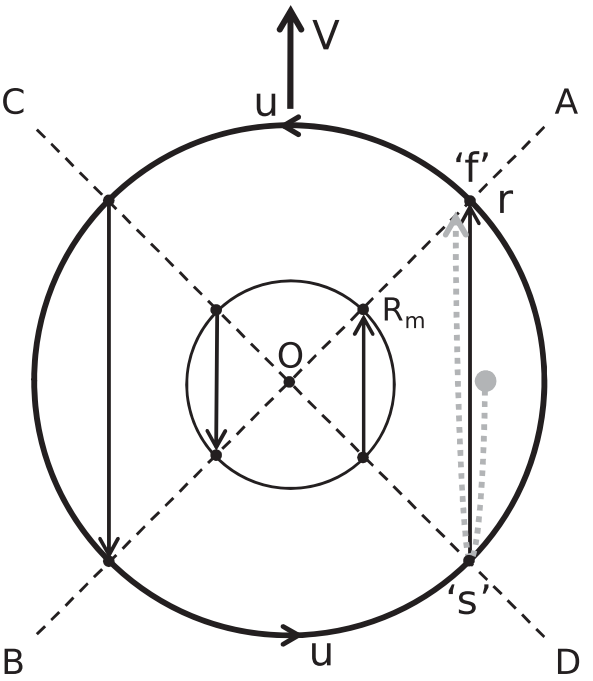

Figure 9. Sketch of wind field in a TC and its "alignment" (straight black solid lines with arrows) for the model simulations. Wave enhancement due the wave trapping is expected along O-A. Wave diminution is expected along O-B due to a reduced duration of wave generation under winds opposing the TC translation direction (indicated by V). Gray dotted line shows schematically trajectory of developing wave train from point of its generation (gray filled circle), to the point where development of wave train is terminated (gray arrow at the end of dotted line).

fetches confined within transects A-B and C-D, Figure 9. For example, wind waves observed at point "f" with radius r, Figure 9, have been developed along the fetch starting from point "s." Length of this fetch is $l_r=\sqrt{2}r$ and it is assumed that the average wind speed generating these waves is $u_r=u(r)$.

Let first consider waves in the right TC sector, where TC translation velocity is aligned with the wind. The inverse age of waves developing in the moving storm area bounded from one (rear) side is given by (A17). Here a simplified 1-D stationary wind field is bounded from both sides. This presumes that relation between dimensionless length (fetch), $\tilde{l}_r=l_r g/u_r^2$, and the critical fetch (see (A18)):

$$\tilde{L}_{cr}=-c_\alpha^{-1/q}\frac{q}{1+q}\alpha_T^{1/q}, \tag{5}$$

should play the key role in the wave development. In (5), $\alpha_T=u_r/2V$ is the inverse age of trapped waves, and q and c_α are constants in the law (2a). If $\tilde{l}_r > \tilde{L}_{cr}$, then wave generation begins at the distance $\tilde{L}_{cr}$ from transect O-D, schematically shown in Figure 9 by a gray dot where wave trajectory begins. Initially, developing waves are "slow," $\alpha > \alpha_T$, and travel backward in the moving coordinate system. Intersecting O-D, the wave group velocity can match the storm translation velocity, $\alpha=\alpha_T$, wave train turning point "s," Figure 9. Developing waves change direction and further start to travel forward in the moving coordinate system, $\alpha < \alpha_T$, increasing their group velocity. Inverse wave age $\alpha_r=\omega_p u_r/g$ and the dimensionless energy $\tilde{e}_r=e_r g^2/u_r^4$ at given radius r along O-A (point "f" where wave development ceases; Figure 9) are given by (A17) and written as:

$$\begin{gathered}(\alpha_r/\alpha_{0r})^{1/q}\left[1-(1+q)^{-1}\alpha_r/\alpha_T\right]=1-\tilde{L}_{cr}/\tilde{l}_r,\\ \tilde{e}_r/\tilde{e}_{0r}=(\alpha_r/\alpha_{0r})^{p/q},\end{gathered} \tag{6}$$

where $\alpha_{0r}=c_\alpha\tilde{l}_r^q$ and $\tilde{e}_{0r}=c_e\tilde{l}_r^p=c_e(\alpha_{0r}/c_\alpha)^{p/q}$ are the reference "expected" wave age and energy for a stationary TC (when $V=0$). The highest waves are then generated if TC parameters (radius, wind, and translation speed) satisfy the condition: $l_r\equiv\sqrt{2}r=(u_r^2/g)\tilde{L}_{cr}$. In this case, (6) gives

$$\begin{gathered}(\alpha_r)_{\min}=(1+q)\alpha_T,\\ (\tilde{e}_r)_{\max}=c_e c_\alpha^{-p/q}(1+q)^{p/q}\alpha_T^{p/q}.\end{gathered} \tag{7}$$

Fully developed seas with wave age $\alpha_r\approx 1$ can thus be generated if the ratio between TC translation and wind speed is about $V/u=(1+q)/2\approx 0.36$. The critical length (5) in this case becomes $\tilde{L}_{cr}\approx 2.3\times10^3$. For wind speed $u=30$ m/s, the TC translation velocity should be about $V\approx 10$m/s, leading to $H_s\approx 20$ m and wavelength $\lambda_p\approx 560$ m, generated at radius $r=2^{-1/2}(u^2/g)\tilde{L}_{cr}\approx 150$ km.

For a fast moving TC, $\tilde{l}_r < \tilde{L}_{cr}$ (which is probably a rare event), developing wind waves are not capable to reach a group velocity to match TC translation. Hence, in a TC moving coordinate system, all waves develop backward, and there are no waves along O-A. In this case, abnormal undergrown seas with relatively low energy appear along transect O-D (Figure 9). Inverse age of these waves follows (A15), where the definition of the integration constant C prescribes the wave generation to start (i.e., $\alpha\to\infty$) at $\tilde{X}=\tilde{l}_r$, leading to:

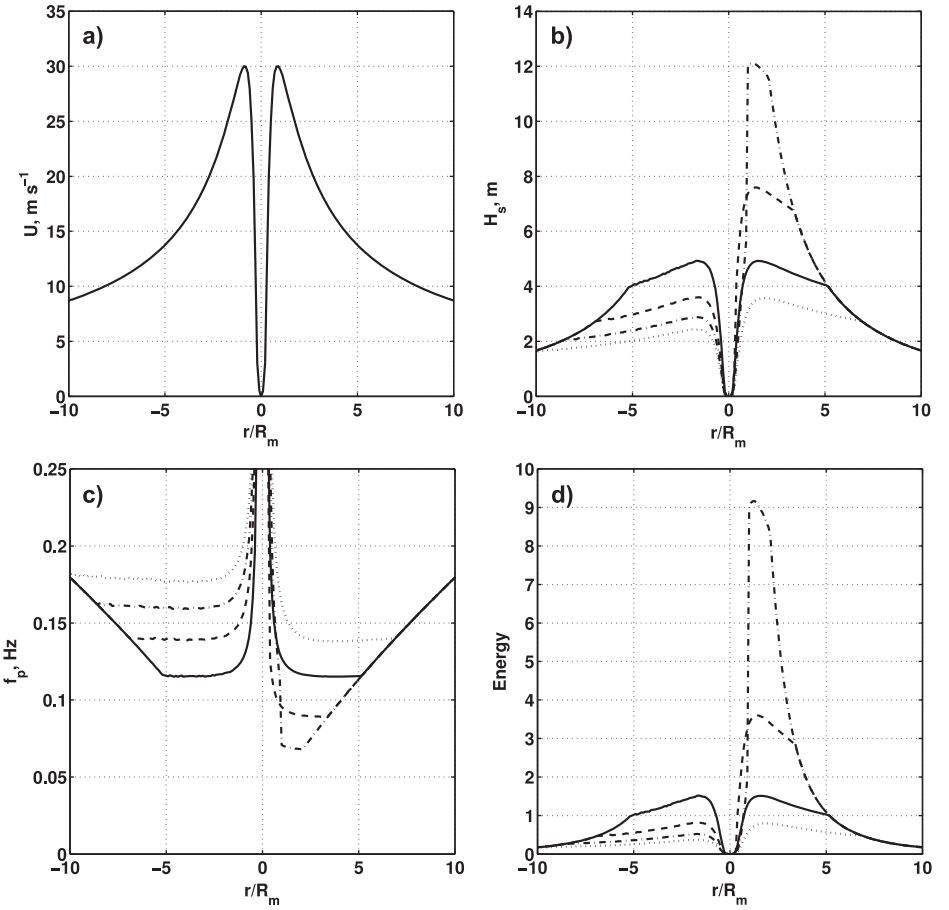

Figure 10. Model distribution of wind wave parameters—(b) significant wave height, H_s, (c) spectral peak frequency, f_p, (d) wave energy along the transect A-B (see sketch in Figure 9) generated by a TC moving with different translation velocities: $V=$ 0 m/s (solid lines), $V=$ 4 m/s (dash lines), $V=$ 8 m/s (dash-dotted lines), and $V=$ 12 m/s (dotted lines). Figure 10a shows wind speed profile defined by (1) with $R_m=$ 50 km, $U_m=$30 m/s. Negative values of r/R_m corresponds to the transect B-O and positive values to transect O-A in Figure 9. Wave parameters for the fast TC with $V=$ 12 m/s shown by dotted lines in the right sector (positive r/R_m) are related to the transect O-D.

$$(\alpha_r/\alpha_{0r})^{1/q}\left[(1+q)^{-1}\alpha_r/\alpha_T-1\right]=1,$$
$$\tilde{e}_r/\tilde{e}_{0r}=(\alpha_r/\alpha_{0r})^{p/q}. \tag{8}$$

In the left sector, the wind direction is opposite to the TC movement. Therefore, wind seas in this area should be less developed, relative to a stationary TC. Wind waves initially generated along transect O-C, Figure 9, further intersect O-B with inverse wave age defined by:

$$(\alpha_r/\alpha_{0r})^{1/q}\left[1+(1+q)^{-1}\alpha_r/\alpha_T\right]=1, \tag{9}$$

which follows from (A20) where we have changed the sign in the square bracket (because $\alpha_T=u_r/2V$ in (9) is positive on definition). In this case waves are less developed compared to stationary TC, $\alpha_r > \alpha_{0r}$, and thus have lower energy: $\tilde{e}_r/\tilde{e}_{0r}=(\alpha_r/\alpha_{0r})^{p/q}$.

Model simulations for an idealized TC, with wind speed profile defined by (1), maximum wind speed $U_m=$ 30 m/s and radius of maximum wind speed $R_m=$ 50 km, and for different TC translation velocities, are shown in Figure 10. For a stationary case, $V=0$, profiles of wind wave parameters along A-B transect (front-right to rear-left quadrant) are symmetrical relative to TC eye. Asymmetry in the wind wave energy and wave frequency distribution between front-right and rear-left quadrants then increases significantly with increasing TC translation velocity. At $V=8$ m/s, asymmetry becomes well evidenced with the front-right quadrant becoming the wave-containment quadrant. At TC translation velocity $V=12$ m/s, the wave energy

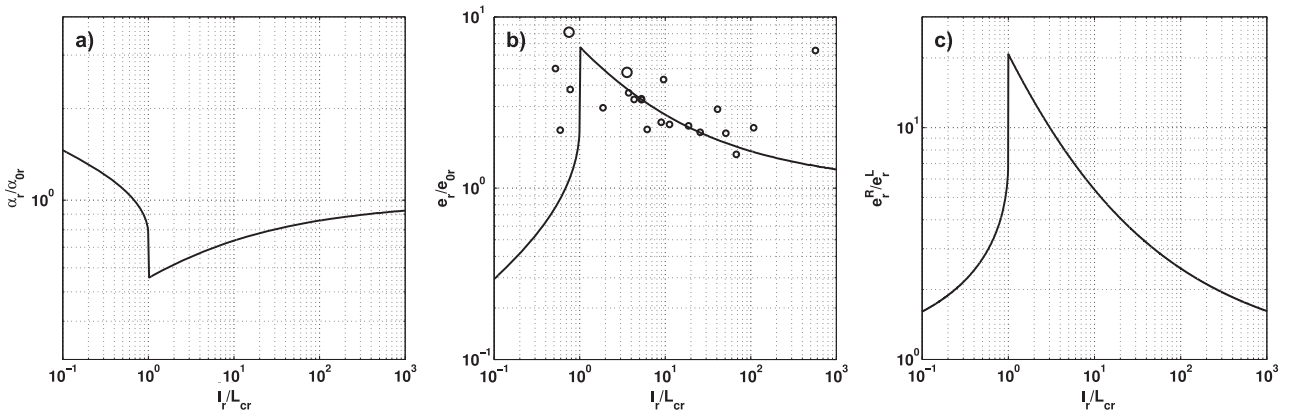

Figure 11. (a) Inverse wave age, (b) energy of waves scaled by their reference values (for stationary TC) in the right sector of TC, and (c) asymmetry coefficient defined as ratio between energy in the right and left sectors. Calculations performed for different combination of TC parameters (translation velocity, wind speed, and radius) all converge into a single curve showing self-similarity of the solution. Small open circles in Figure 11b show the enhancement factor derived from observations of typhoons listed in Table 1. Large open circles show the enhancement factor derived from altimeter measurements of TCs Isabel and Julia.

in the front-right quadrant is strongly reduced. The TC is too fast to trap leading waves, and wind waves develop backward, with group velocity less than the TC translation velocity.

3.2. Simulation of Observed Wave Energy Profiles

The proposed analytical development described above has been applied to the selected cases, Figures 4–7. Wind waves are simulated using both altimeter-wind speed and model wind speed. For almost symmetrical wind field, like TCs Isabel, Figure 4, and Songda, Figure 5, the model quantitatively reproduces measured energy profiles. Though differences between the model-wind and altimeter-wind profiles are noticeable, the energy ratios between the front-right and the rear-left quadrants are similar for both wind sources.

Wave energy distribution for TCs Muifa and Prapiroon also exhibits marked asymmetry. According to altimeter-wind speed estimates, this, at least its major part, is likely a consequence of the wind speed difference between front-right and rear-left quadrants. Inclusion of the TC movement effect amplifies the wave asymmetry, which however becomes larger than measured one. Model simulations for a symmetrical model-wind input can reproduce measured asymmetries only related to the wave trapping effect.

3.3. Enhancement Factor

From a practical perspective, it can be crucial to rapidly assess wind wave potential enhancement in the front-right quadrant of a TC. At each point along the O-A transect, Figure 9, where condition $\tilde{I}_r > \tilde{L}_{cr}$ is fulfilled, the wave age and wave energy can be simply determined solving (6). If $\tilde{I}_r < \tilde{L}_{cr}$, corresponding to a fast moving TC, the wind waves leave the TC (with wave age defined by (8)) through its rear-right quadrant, i.e., through transect O-D, Figure 9, and wave energy along O-A is negligible.

Inverse wave age and energy of wind waves along transect O-A (if $\tilde{I}_r/\tilde{L}_{cr} > 1$) and O-D (if $\tilde{I}_r/\tilde{L}_{cr} < 1$) scaled by their reference values (for a stationary TC) are shown in Figures 11a and 11b, as a function of radius-dependent fetch $\tilde{I}_r = \sqrt{2}r$ scaled by the critical fetch $\tilde{L}_{cr}$. Calculations are performed for a wide range of wind speeds (from 25 to 70 m/s), TC translation velocities (from 0 to 20 m/s) and radii from the TC eye (from 10 to 500 km). As obtained, all model curves converge to a single one. Thus, derived solutions (6) and (8) are unique functions of the dimensionless parameter $\tilde{I}_r/\tilde{L}_{cr}$. This is not surprising because α_r/α_T, as it follows from (3) and (5), is proportional to: $\alpha_r/\alpha_T \propto (\alpha_r/\alpha_0)(\tilde{I}_r/\tilde{L}_{cr})^q$. Hence, relations (6) and (8) represent a self-similar solution for waves generated by moving TC:

$$\begin{aligned} \alpha_r/\alpha_0 &= \varphi_\alpha\left(\tilde{I}_r/\tilde{L}_{cr}\right), \\ \tilde{e}_r/\tilde{e}_0 &= \varphi_e\left(\tilde{I}_r/\tilde{L}_{cr}\right), \end{aligned} \tag{10}$$

where φ_a and φ_e are some universal functions. Following this reasoning, one may find that wave age (9) and the energy in the left sector (along transect O-B) scaled by their reference values are also a unique

functions of $\tilde{I}_r/\tilde{L}_{cr}$, and can be represented in form of self-similar function (10). Asymmetry of wind-waves, e.g., the ratio of wave energy in the right sector to the energy in the left one, can then be the most striking feature of the wavefield in TC. Figure 11c shows coefficient of asymmetry defined as the ratio of the energy $\tilde{e}_r$ along O-A (if $\tilde{I}_r/\tilde{L}_{cr} > 1$) and O-D (if $\tilde{I}_r/\tilde{L}_{cr} < 1$), $\tilde{e}_r^R$, to the energy $\tilde{e}_r$ along transect O-B, $\tilde{e}_r^L$, as a function of $\tilde{I}_r/\tilde{L}_{cr}$. When a TC is in "resonance" with wind seas, i.e., if $\tilde{I}_r/\tilde{L}_{cr} \approx 1$, asymmetry coefficients, $\tilde{e}_r^R/\tilde{e}_r^L$ can attain large values, up to $\tilde{e}_r^R/\tilde{e}_r^L \approx 20$.

All TCs listed in Table 1 have been used to assess the amplification factor. These altimeter measurements all crossed the TC front-right quadrant, i.e., the area where largest waves are expected. For each of the tracks, we determine the local maximum of H_s (as a mean of 3–5 maximal observed values of H_s), radius of its location, local wind speed (using model (1) for typhoons, and measured altimeter wind for TCs Isabel and Julia), and critical fetch (5). All collected data are plotted in Figure 11b and confirm the amplification of the wave energy in the front-right quadrant, consistent with the model prediction.

At a given local fetch, $I_r = \sqrt{2}r$, which is close to the critical fetch, $\tilde{I}_r \approx \tilde{L}_{cr}$, wind waves generated by TC are thus trapped. In "measurable" variables, the criterion for generation of trapped abnormal waves thus reads:

$$gr/u_r^2 \approx c_T (u_r/V)^{1/q}, \tag{11}$$

where $c_T = -2^{-1/2}(2c_\alpha)^{-1/q} q/(1+q)$ which is equal to $c_T = 6.5\times10^4$ using the growth rate law (2) and constants suggested by *Babanin and Soloviev* [1998]. In this case, see (7), inverse wave age and energy of abnormal waves in the front-right quadrant are:

$$\begin{aligned} \alpha_{\min} &\approx \left(\frac{1+q}{2}\right)\frac{u_r}{V}, \\ \tilde{e}_{\max} &\approx c_T^e \left(\frac{u_r}{V}\right)^{p/q}, \end{aligned} \tag{12}$$

where $c_T^e = c_e c_\alpha^{-p/q}[(1+q)/2]^{p/q}$ which is equal to $c_T^e = 7.8\times10^{-2}$ for the growth rate constants suggested by *Babanin and Soloviev* [1998]. To generate such abnormal waves, TC forcing conditions (wind speed and translation velocity) must be quasi stationary during a time period T:

$$\begin{aligned} \frac{gT}{u_r} &\approx \frac{2c_a}{1+q}\left(2\tilde{L}_{cr}\right)^{1+q} \\ &= c_T^t \left(\frac{u_r}{V}\right)^{(1+q)/q}, \end{aligned} \tag{13}$$

where $c_T^t = 2^{1+q-1/q} c_\alpha^{-1/q}(1+q)^{-2-q}(-q)^{1+q}$ which is equal to $c_T^t = 2.7\times10^5$. Using relations (12), the spectral peak group velocity, c_g, becomes

$$c_g = V/(1+q), \tag{14}$$

with the corresponding wavelength of the spectral peak:

$$\lambda_p = \frac{2\pi}{g}\left(\frac{2V}{1+q}\right)^2, \tag{15}$$

and significant wave height:

$$\begin{aligned} H_s^{\max} &= 4(c_T^e)^{1/2}\left(\frac{u_r}{V}\right)^{p/2q}\frac{u^2}{g} \\ &= 4(c_T^e)^{1/2} g^{-1} u_r^{(4q+p)/2q} V^{-p/2q}. \end{aligned} \tag{16}$$

Remarkably, the group velocity and wavelength of emanating waves, outrunning the TC motion, are wind independent. These parameters solely relate to the TC translation velocity. Considering $p/2q \approx -1.6$, the resulting significant wave height is then only weakly dependent on the wind forcing, $\propto u^{0.38}$, and more strongly depends on the translation velocity, $\propto V^{1.6}$. As an alternative, if we adopt *Toba* [1972] constants, $p = 3/4$ and $q = -1/4$, then $p/2q \approx -3/2$. The wind speed and translation velocity dependencies become $\propto u^{1/2}$ and $\propto V^{3/2}$, respectively, i.e., close to the empirical predictions.

As already noticed, the wind wavefield asymmetry (ratio of the wave energy between right, e_r^R, and left, e_r^L, sectors), at near-resonance conditions, $\tilde{I}_r \approx \tilde{L}_{cr}$, is quite large (see Figure 11c). To quantify the asymmetry coefficient, e_r^R/e_r^L, we express α_r/α_{0r} in the right sector (using (5) and (7)) as: $\alpha_r^R/\alpha_{0r}=(1+q)^{1+q}(-q)^{-q} \equiv a_0$, where a_0 is related to the enhancement factor, e_r^R/e_{0r}, as: $e_r^R/e_{0r}=a_0^{p/q}$. The similar ratio for the left sector can be derived from (9) and is approximately: $\alpha_r^L/\alpha_{0r}=a_0^{q/(1+q)}-a_0 q/(1+q)$. Using (A5a), we obtain the following expression for the wind wavefield asymmetry coefficient at the resonance:

$$e_r^R/e_r^L=\left(\alpha_r^R/\alpha_r^L\right)^{-p/q}=\left[a_0^{-1/(1+q)}-q/(1+q)\right]^{-p/q}. \tag{17}$$

Using empirical constants by *Babanin and Soloviev* [1998], coefficient of asymmetry is $e_r^R/e_r^L \approx 23$ for energy, and about $H_s^R/H_s^L \approx 4.8$ for the wave heights.

Considering $V=$ 8 m/s, the group velocity and wavelength of outrunning waves are predicted to be about $c_g=$ 11 m/s and $\lambda_p=$ 310 m, respectively. For wind speed $u_r=$30 m/s, $V/u_r=0.27$ and $H_s \approx$ 12m, to exceed by a factor 2.5 the significant wave height, $H_s \approx$ 5m, of waves generated by a stationary TC (same radius and wind speed). However, we remind that abnormal waves can only be generated if the TC radius satisfies criterion (11). For this specific case, this corresponds to $r \approx$ 50km. Moreover, quasi-stationary TC conditions shall be stable within $T_r \approx$ 7 h (see equation (13)).

Altimeter measurements along the track crossing TC Julia close to its eye, Figure 12, provide an impressive example of the generation of abnormal trapped waves in real conditions. Wind speed and wave energy profiles along the altimeter track are shown in Figure 13. TC Julia was moving quite rapidly, with estimated translation velocity (derived from TC best-track record, Figure 12) about $V \approx$ 8 m/s. The derived altimeter wind profile, Figure 13, confirms a ground track crossing at distance $r < R_m$ from the eye. This estimated wind profile further helps to directly infer the radius of the maximum wind. From trivial geometric analysis, we indeed have

$$R_m=(d/2)/\sqrt{1-u_{\min}^2/U_m^2}, \tag{18}$$

where d is the distance between local wind speed maxima, $u_{\min}$ is the measured wind speed minimum, and U_m is the measured wind speed maximum. From the data shown in Figure 13, $u_{\min} \approx$ 15 m/s, $d \approx$ 90 km, and $U_m \approx$25 m/s, giving an estimation of the radius of maximum wind speed $R_m \approx$ 55 km. To fulfill criterion (11), the radius of TC Julia moving with $V \approx$ 8 m/s and U_m within the range from $U_m=$ 25 m/s to $U_m=$ 30 m/s should be in the range 50 km $<R_m<$ 66 km, which overlaps the TC radius estimated from the altimeter wind profile. Thus, wind waves generated within the TC Julia right sector are likely the most possible energetic trapped waves, with energy given by (12), which should be in the range 8 m$^2 < e <$ 9 m^2, or in terms of H_s, in the range 11 m $<H_s<$ 12 m. As compared, this expectation is consistent with the altimeter-derived, markedly asymmetrical, profile of maximum energy, Figure 13. Model simulations of the wave energy (with altimeter wind speed as the input parameter) for different translation velocities overlapping observed one, are shown in Figure 13. These simulations are consistent with the measurements reproducing observed asymmetry of wind waves and their abnormal energy.

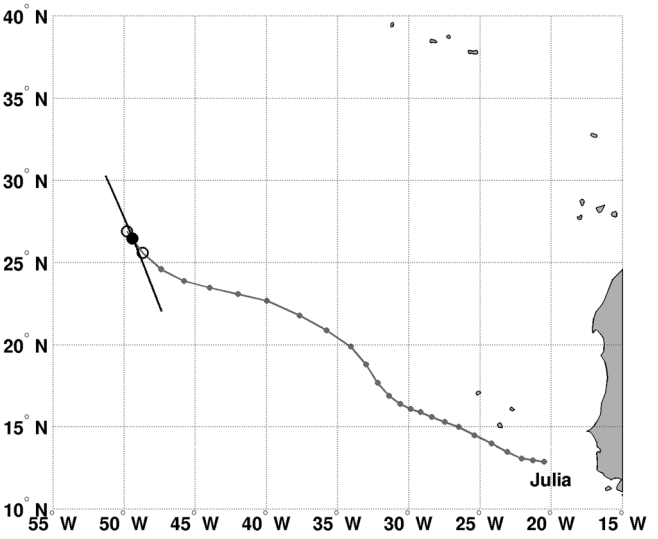

Figure 12. TC Julia best track as determined by NOAA HURDAT, and the altimeter ground track crossing TC Julia close to the eye. Open circles indicate TC locations before and after altimeter crossing time, and black dots indicate interpolated TC location at the crossing time.

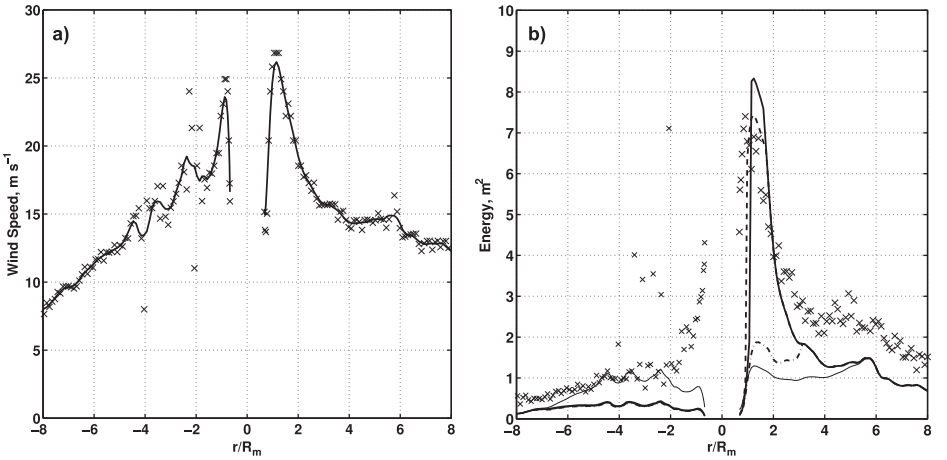

Figure 13. TC Julia. (a) Wind speed measured by the altimeter (symbols) and smoothed altimeter wind speed (gray line). (b) Wave energy measured by the altimeter (symbols), the reference (if TC is stationary) wave energy profile corresponding to the altimeter wind speed (thin solid line), and the model wave energy profiles along the transect from front-right to rear-left quadrants calculated on (6) and (9) using altimeter wind speed for different translation velocity $V = 7.5$ m/s (dashed line), $V = 8$ m/s (solid line), and $V = 8.5$ m/s (dash-dotted line). At $V = 8.5$ m/s, TC is too fast to generate trapped waves, therefore model wave energy shown for this case corresponds to the rear-right quadrant. $R_m = 55$ km.

From this analysis, the fetch-law principle applied to a rapidly moving extreme event over a relatively limited horizontal extension appears robust and sufficient to provide valuable sea state information.

4. Discussion

These results comfort the initial assumption about the essential role of nonlinear wave-wave interactions to continually shape and stabilize the energy containing part of the wave spectra. Even under extreme conditions, resulting self-similar laws appear robust and can efficiently be used to determine the spatiotemporal evolution of the spectral peak and the associated wave-age of the wavefield. This must come from a rapid adjustment of the energy containing part of the spectrum to atmospheric forcing conditions essentially balanced at smaller scales. As such, these developments are not strictly restricted to uniform and stationary wind conditions, and/or symmetrical TC forcing fields.

In that context, using geostationary observations to evaluate the TC motion and its general dimension characteristics, plausible TC-induced wave (and surge) hazards can be rapidly estimated, depending on the TC evaluated strength, using the criterion $gr/u_r^2 \approx c_T(u_r/V)^{1/q}$. Given this wave enhancement criterion for moving extreme events, and its associated time scale interval, abnormal wave energy amplification shall further not necessarily correspond to the maximum wind radial distance. Lower and more sustained winds at larger distance from the eye will more likely fulfill the wave enhancement criterion. Accordingly, the possible underrepresentation of the most intense wind speeds in satellite wind measurements, due to lack of sensitivity and/or medium to low-resolution constraints, may not be as crucial as initially anticipated.

Wave records from satellite altimetry can then provide a robust means to further analyze passed TCs and help to validate the proposed development. Altimeter measurements can then help quantify wave hindcast models and the wind reanalyses used to drive these wave models. The availability of more than 20 years of dual-frequency altimeter measurements, together with the high-resolution synthetic aperture radar (SAR) measurements, with continuous improvement of TC intensities estimates, is a motivation to further revisit the potential of the self-similarity principle and associated fetch laws. In particular, waves with periods larger than 14 s (wavelength of about 300 m) can now be routinely observed to often propagate all the way across ocean basins from the area of high winds that generated them [e.g., *Collard et al*., 2009; *Husson et al*., 2012]. To further complement the sparse coverage provided by satellite altimeters, in situ measurements by buoys and seismic noise records from the Global Seismic Network, can also be used especially in the Southern Hemisphere [e.g., *Barruol et al*., 2006]. To note, seismic stations are now analyzed in real time for local marine forecasts and high surf advisories.

5. Conclusion

In this paper, the self-similarity aspect of wind wave growth is exploited and generalized for moving conditions. A simplified analytical model is derived to efficiently describe the wave energy distribution along the main transects of a moving extreme weather event. Such a model essentially builds on the existence of a strongly dominant single spectral mode in a given quadrant of the storm.

Satellite altimeter measurements, together with TC intensities estimates, are used to assess the proposed formulations. Compared to satellite altimeter measurements, the proposed analytical solutions for the wave energy distribution are in convincing agreement. For almost symmetrical wind field, the model quantitatively reproduces measured profiles of the wave energy with significant asymmetry between the wave-containment front-right quadrant and the rear-left quadrant where wave energy is remarkably damped. Though the differences between model-wind and altimeter-wind profiles are noticeable, the energy ratios between the front-right and the rear-left quadrants are similar for both wind sources.

As estimated from satellite measurements, the effective fetch, following self-similarity laws, first linearly grows with increasing V/u. For relatively slow TCs, $0.1 \leq V/u \leq 0.2$, results are in agreement with the effective fetch proposed by *Young* [2013]. As further inferred, the effective fetch for a stationary TC, i.e., $V \approx 0$, tends to $x_{ef} \approx 1.4r$, with r, the radial distance from the eye.

As proposed, key is then to compare the dimensionless radius-related fetch, $\tilde{l}_r = \sqrt{2}rg/u_r^2$, with a critical value, $\tilde{L}_{cr}$, essentially governed by V/u, the ratio between the translating velocity and the wind speed. This criterion is given by (11), to rapidly indicate if partial resonance effects can take place to increase the effective fetch and duration of the wave-growth process in the direction of the TC's motion, i.e., the wave trapping phenomenon. If forced during a sufficient time interval, defined by (13), over which these trapped waves are exposed to almost constant environmental conditions, i.e., quasi-constant V and u_r, large amplification of the wave energy prescribed by (12) will occur. Remarkably, the group velocity and corresponding wavelength of the emanating wave systems, outrunning the TC motion, become wind speed independent. Indeed, these parameters shall solely relate to the translating velocity (equations (14) and (15)). The resulting significant wave height then only weakly depends on wind speed, and more strongly on TC translation velocity (equation (16)). As motivated, this derivation is not intended to compete with advanced wind wave generation models. But, as analytically developed, this will simply enable a rapid evaluation to further document the general characteristics of each storm, especially the expected wavefield asymmetry.

In particular, estimated nondimensional fetch close to or larger than the critical value will indicate that the resonance effect will be large with a rightward wave energy marked enhancement. The criterion can further be used for future investigations concerned with TC-induced vertical mixing [e.g., *Grodsky et al*., 2012], climatology completeness [e.g., *Knaff et al*., 2013; *Smirnova et al*., 2015], radiating swell determination and dissipation estimation [e.g., *Ardhuin et al*., 2009; *Young et al*., 2013], but also investigations concerned by the local sea state impact on microwave measurements to infer surface extreme wind speeds from passive instruments [*Uhlhorn and Black*, 2003; *Reul et al*., 2012; *Zabolotskikh et al*., 2013, 2015] and future bistatic L-band Cyclone Global Navigation Satellite System (i.e., CYGNSS [*Ruf et al*., 2013]).

Finally, owing to the essential role of nonlinear wave-wave interactions to continually shape and stabilize the energy containing part of the wave spectrum, the proposed model can further dwell on recently proposed universal relationships put forward by Zakharov and coauthors [*Zakharov et al*., 2015] to include nonstationary conditions and different wave-growth regimes. Future investigations will also be dedicated to propose a 2-D extension to the present analysis.

Appendix

A1. Basic Relations

A1.1. Fetch and Duration-Limited Laws

The suggested model is an extension of the self-similarity theory for wind-driven wave generation by a moving TC. Following the similarity concept, growth of wind waves (their energy, e, spectral peak frequency, ω_p) can be completely described using a length scale associated with the fetch, x, or time duration, t, and wind velocity, u. Hereinafter, we use wind speed at 10 m height. Scaling arguments lead to define

nondimensional fetch, $\tilde{x}=xg/u^2$, dimensionless duration, $\tilde{t}=tg/u$, wave energy, $\tilde{e}=eg^2/u^4$, and spectral peak frequency $\tilde{\omega}_p=\omega_p u/g$, where g is the gravity acceleration. The latter is equivalent to inverse wave age, $\alpha=u/c_p$, c_p is phase velocity of the spectral peak waves [*Kitaigorodskii*, 1962]. Significant wave height, H_s, is related to the energy as $H_s=4\sqrt{e}$. According to the self-similarity theory, the dimensionless wave energy and spectral peak frequency are universal functions of the fetch, $\tilde{\omega}_p=\tilde{\omega}_p(\tilde{x})$ and $\tilde{e}=\tilde{e}(\tilde{x})$, and duration, $\tilde{\omega}_p=\tilde{\omega}_p(\tilde{t})$, $\tilde{e}=\tilde{e}(\tilde{t})$. The universal functions are usually expressed as power laws

$$\tilde{\omega}_p \equiv \alpha=c_\alpha \tilde{x}^q, \tag{A1a}$$

$$\tilde{e}=c_e \tilde{x}^p, \tag{A1b}$$

for the fetch-limited conditions and

$$\tilde{\omega}_p \equiv \alpha=c_{\alpha t} \tilde{t}^{q_t}, \tag{A2a}$$

$$\tilde{e}=c_{et} \tilde{x}^{p_t}, \tag{A2b}$$

for the duration-limited ones. Such power laws had demonstrated their efficiency to interpret the measurements (see, e.g., review by *Badulin et al*. [2007]). Although the exponents and preexponents in (A1) and (A2) should be universal constants, their empirical estimates demonstrate broad variety, e.g., the fetch-law exponents p and q vary in the range: $0.7<p<1.1$, $-0.33<q<-0.23$, and constants c_e and c_α vary as: $0.7\times10^{-7}<c_e<18.9\times10^{-7}$, $10.4<c_\alpha<22.7$ [see *Badulin et al*., 2007, Table 2]. Scatter of the empirical constants is generally treated with complexity of the wind field, impact of the atmospheric stratification, gustiness in the wind, etc. *Badulin et al*. [2007] also argued that in spite of its efficiency, this approach (based on dimensional analysis) has a restricted applicability, and does not provide a deep insight into the physics of the wind-driven seas.

A breakthrough in understanding of the physics of the growth of wind-seas had been made in works by *Zakharov* [2005], *Badulin et al*. [2007], *Gagnaire-Renou et al*. [2011], and *Zakharov et al*. [2015]. This new approach is based on the asymptotic solutions of the kinetic equation:

$$\partial E/\partial t+c_{gj}\partial E/\partial x_j=S \equiv S_W+S_D+S_N, \tag{A3}$$

where c_{gj} is the group velocity, and S the total energy source, consisting of the nonlinear transfer term (collision integral), S_N, a wind forcing (S_W) and dissipation (S_D) terms which are usually adjusted functions. Assuming the leading role of nonlinear transfer term, a family of self-similar solutions corresponding to the power laws (A1) and (A2) had been obtained. These solutions, both for the fetch and the duration-limited wave development, obey the fundamental law, which provides the deterministic links between the exponents in (A1) and (A2):

$$p=(10q-1)/2, \quad p_t=(9q_t-1)/2. \tag{A4}$$

The exponents, being linked by (A4), are dependent on stage of the wave-development, characterized by constancy of (i) the nonlinear momentum flux (very young seas), (ii) the energy flux (growing seas, regime of the maximal wave energy production), and (iii) the wave-action flux (mature seas) (see *Badulin et al*. [2007] and *Gagnaire-Renou et al*. [2011] for more details). The fetch-law exponents p and q for each of these stages are (i) $p=1$, $q=-3/10$ (in line with *Hasselmann et al*. [1976]); (ii) $p=3/4$, $q=-1/4$ (in line with *Toba* [1972]); and (iii) $p=4/7$, $q=-3/14$ (in line with *Zakharov and Zaslavsky* [1983]).

To note, the self-similar solutions (A1) and (A2) can be represented as one-parametric expression relating the dimensionless energy to the wave age:

$$\tilde{e}=c_e(\alpha/c_\alpha)^{p/q}, \tag{A5a}$$

$$\tilde{e}=c_{et}(\alpha/c_{\alpha t})^{p_t/q_t}. \tag{A5b}$$

Remarkably, the self-similarity between dimensionless energy and wave age, for both the fetch (A5a) and the duration (A5b), then dictates that the ratio of the exponents in (A5a) and (A5b) must be the same, i.e., $p/q=p_t/q_t$. Therefore, the growth of wind seas, either in space or in time, is described by a one-parametric function (A5) for any stage of the wave development [see *Gagnaire-Renou et al*., 2011, Table 1].

A1.2. Choice of Empirical Parameterization

Badulin et al. [2007] reviewed empirical dependencies collected in fetch-limited experiments over the past 50 years, and selected those that were most closely approaching the theoretical predictions based on weakly turbulent scaling. Among them, empirical fetch laws suggested by *Babanin and Soloviev* [1998] had been selected. In terms of (A1), the constants of their empirical relations are: $c_e=4.41\times10^{-7}$, $c_a=15.14$, $q=-0.275$, and $p=0.89$. For this case, the exponent in the self-similar dependence of wave energy on wave age (A5a), p/q, is about $p/q\approx-3.2$ that is close to $p/q=-3$ following from both *Toba* [1972] law and the weakly turbulent scaling predictions. We adopt herein *Babanin and Soloviev* [1998] empirical relations as a reference one. However, we restrict their validity by condition $\alpha\geq1$ assuming that: $\tilde{e}=c_e c_\alpha^{-p/q}\alpha^{p/q}$ at $\alpha\geq1$, and $\tilde{e}=c_e c_\alpha^{-p/q}$ at $0.83<\alpha<1$. At $\alpha=1$, relation (A5a) with the reference constants gives $\tilde{e}=2.9\times10^{-3}$, or in terms of dimensionless significant wave height $\tilde{H}_s=0.22$, that corresponds to the fully developed seas. In "reality," there should be a smooth transition from growing seas toward fully developed ones, i.e., in the mature seas (with α around 1), and q should smoothly tend to $q=0$ at $\alpha=0.83$. Notice that such trend is predicted by weak turbulent scaling (regime of the constant wave-action flux) [*Gagnaire-Renou et al*., 2011, Figure 10]. However, for the sake of simplicity, we ignore accounting for such transition, limiting growth of the wave energy by "true" classical Pierson-Moskowitz threshold level, $\tilde{H}_s=0.22$. As an "alternative," the fetch laws based on weakly turbulent scaling for constant energy flux, the regime of the maximal wave energy production (also corresponding to 3/2-law by *Toba* [1972]) is also considered.

A1.3. Equation for the Space-Time Evolution

Considering waves generated by a moving TC, we generalize the "idealized" fetch (A1) or duration (A2) laws to simulate wind wave development, both in space and in time under varying conditions. We assume that in this case, the energy of wind waves still obey the self-similarity, in sense that the dimensionless wave energy is completely defined by wave age (equation (A5)). We then only must modify fetch (A1a) and duration (A2a) laws to introduce a consistent description of the variability of the dimensionless peak frequency under the varying action of wind forcing in both space and time. *Dysthe and Harbitz* [1987] suggested to use space-to-time transformation, $dx/dt=c_g$, to extend kinematic law (A1a) on the case of waves generation by polar lows. This idea was followed and implemented by *Bowyer and MacAfee* [2005], with a numerical Lagrangian trapped fetch wave-model for operational applications.

In the present study, we suggest an extension of the weakly turbulent scaling approach to derive equation for the spectral peak frequency evolution using the energy balance equation (A3). To that end, we first approximate the wave spectrum around the peak, $\omega=\omega_p$, by:

$$E(\omega)=E(\omega_p)+(1/2)E''_\omega(\omega-\omega_p)^2. \tag{A6}$$

Hereinafter prime (double prime) over any quantity denotes first (second) derivative with variable indicated as subscript, e.g., $E''_\omega=\partial^2E/\partial\omega^2$. From (A3) derivation with respect to ω and substitution of (A6), the following equation describes the spectral peak frequency evolution:

$$\partial\omega_p/\partial t+(1-\Delta)c_g\partial\omega_p/\partial x=-\left(S'_\omega/E''_\omega\right)_{\omega=\omega_p}, \tag{A7}$$

where $\Delta=\left(\omega_p E'_{\omega_p}\right)/\left(\omega^2E''_\omega\right)|_{\omega=\omega_p}$ is a parameter describing the influence of the spectrum shape on the kinematics of the spectral frequency. Numerical estimates of this parameter for the empirical JONSWAP-spectra (not shown here) indicated that Δ is of order $O(0.1)$, and thus further omitted. Notice, that according to (A7), rate of the spectral peak downshift is proportional to the derivative of the energy source with respect to ω. Since, under growing sea conditions, both the wind forcing and the dissipation have local maxima in the vicinity of the spectrum peak, $\omega=\omega_p$, the only mechanism leading to the spectral peak downshift is the nonlinear wave interactions.

Following the self-similarity approach, right-hand side of (A7) at $\omega=\omega_p$ can be expressed as: $\left(S'_\omega/E''_\omega\right)_{\omega=\omega_p}=-(g/u)^2\varphi(\alpha)$, where $\varphi(\alpha)$ is a dimensionless universal function of the wave age. Then (A7) reads:

$$\partial\omega_p/\partial t+c_g\partial\omega_p/\partial x=(g/u)^2\varphi(\alpha). \tag{A8}$$

This equation corresponds to the development by *Hasselmann et al*. [1976, equation (4.11)], which is also in line with self-similar solutions introduced by *Badulin et al*. [2007], *Gagnaire-Renou et al*. [2011], and *Zakharov et al*. [2015].

We define $\varphi(\alpha)$ so that (A8) for stationary conditions ($\partial\omega_p/\partial t=0$) would provide a "known" fetch law (A1a), hence:

$$\varphi(\alpha)=1/2qc_\alpha^{1/q}\alpha^{-1/q}. \tag{A9}$$

Equation (A8) with (A9) generalizes the fetch law (A1a) on other conditions. In particular, this equation relates the duration law (A2a) to the fetch law (A1a). Solution of (A8) (with $\partial\omega_p/\partial x=0$) gives the duration laws in form of (A2) where the exponent and preexponent are linked with the fetch-law constants as:

$$q_t=q/(1+q), \qquad c_{\alpha t}=\left[c_\alpha^{1/q}(1+q)/2\right]^{q/(1+q)}. \tag{A10}$$

This is in line with general findings [*Badulin et al*., 2007; *Zakharov et al*., 2015] derived from first principles.

A2. Moving Wind

Let now find solution of equation (A9) with (A10) for a moving wind field described by

$$u(x,t)=uH(x-Vt), \tag{A11}$$

where H is the Heaviside function (defined as $H(y)=1$ if $y\geq 0$, and $H(y)=0$ if $y<0$), V is the wind field translation velocity, and u is a constant wind speed in x direction. In coordinate system following the storm,

$$X=x-Vt, \tag{A12}$$

equation (A8) becomes:

$$(c_g-V)\partial\omega_p/\partial X=(g/u)^2\varphi(\alpha). \tag{A13}$$

Taking into account (A9), this equation can be rewritten as:

$$\frac{\partial\alpha}{\partial\tilde{X}}=qc_\alpha^{1/q}\alpha^{(1-1/q)}\left(\frac{u}{u-2\alpha V}\right), \tag{A14}$$

where $\tilde{X}=Xg/u^2$. After integration, we arrive at:

$$\alpha^{1/q}\left[1-2(V/u)(1+q)^{-1}\alpha\right]=c_\alpha^{1/q}\tilde{X}+C, \tag{A15}$$

where C is an integration constant. If $V=0$, a stationary storm, (A15) with $C=0$ reduces to (A1a).

First we consider a case when storm translation velocity is aligned with the wind, i.e., $V>0$. To describe the growth of waves traveling forward (in coordinate system following the storm), constant C in (A15) is deduced to equalize the spectral peak group velocity, c_g^p, to the translation velocity, $c_g^p=V$, at $\tilde{X}=0$. In terms of wave age, this condition reads:

$$\alpha_T=u/2V, \tag{A16}$$

where α_T is hereinafter termed the inverse wave age of trapped waves. Then (A15) is:

$$\alpha^{1/q}[1+q-\alpha/\alpha_T]-q\alpha_T^{1/q}=(1+q)c_\alpha^{1/q}\tilde{X}. \tag{A17}$$

Except for the waves traveling forward (with decreasing $\alpha\leq\alpha_T$), equation (A17) also possesses solution for younger waves, with $\alpha\geq\alpha_T$, which are generated inside the storm area and travel backward (in coordinate system following the storm). Position of their generation, $\tilde{L}_{cr}$ (hereinafter the critical fetch), can be found from (A17) as value of $\tilde{X}$ where $\alpha\to\infty$:

$$\tilde{L}_{cr}=-c_\alpha^{-1/q}\frac{q}{1+q}\alpha_T^{1/q}. \tag{A18}$$

For the stationary storm, $V=0$, critical fetch is $\tilde{L}_{cr}=0$. Using definition (A18), relation (A17) becomes:

$$\alpha^{1/q}\left[1-(1+q)^{-1}\alpha/\alpha_T\right]=c_\alpha^{1/q}(\tilde{X}-\tilde{L}_{cr}). \tag{A19}$$

Therefore, the growth of wind waves inside a moving storm can be described as follows. Wave generation begins at $\tilde{X}=\tilde{L}_{cr}$. On the initial stage, developing waves are relatively "slow," $\alpha>\alpha_T$. Thus, "young" growing

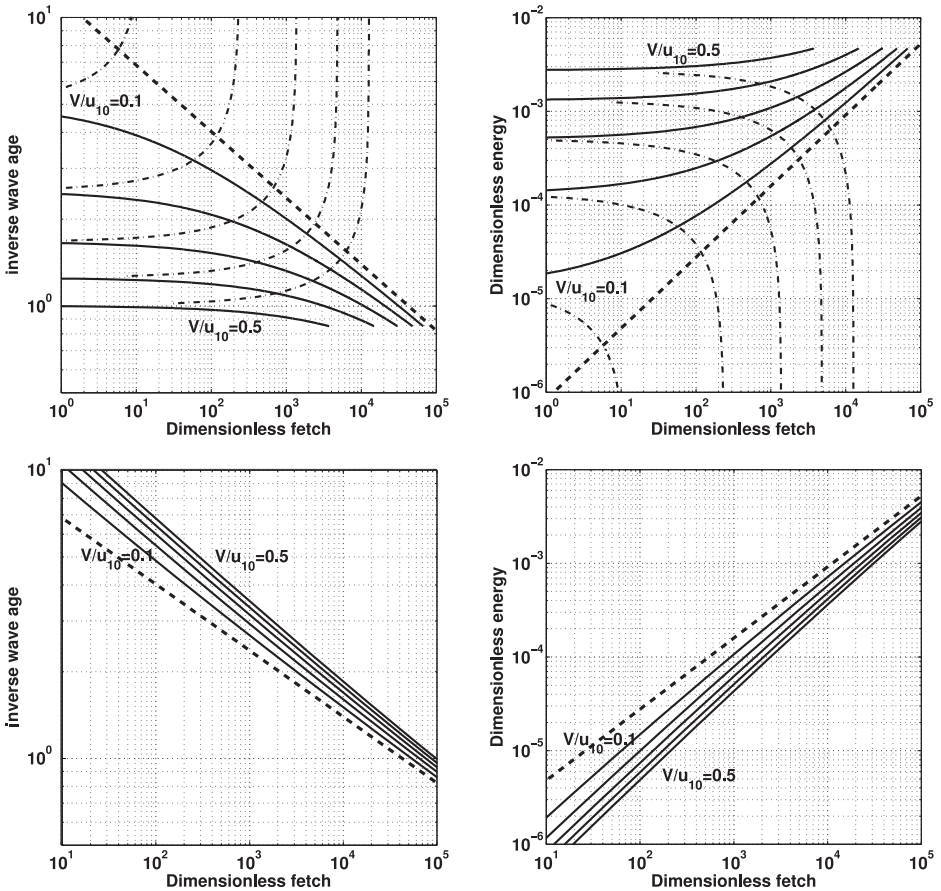

Figure A1. Inverse wave age and dimensionless energy for different dimensionless advance velocities V/u from 0.1 to 0.5. (top row) Translation velocity is aligned with the wind velocity; (bottom row) translation velocity is opposite to the wind velocity. Thick dash lines show the reference calculations ($V=0$). Solid lines in the top row show the forward wave system, and the dash-dotted lines show the backward wave system at different V/u. Solid lines in the lower row show inverse wave age and energy at different V/u.

waves travel backward while at the rear storm boundary, $\tilde{X}=0$, the group velocity has attained the storm translation velocity ($\alpha=\alpha_T$). This boundary $\tilde{X}=0$ is thus a turning point where growing wave trains change direction (from backward to forward). Further, waves develop as the forward waves (with $\alpha < \alpha_T$) increasing their group velocity.

Growth rate curves calculated using (A5a) and (A19) (with parameters suggested by *Babanin and Soloviev* [1998]) for different storm translation velocities are shown in Figure A1. Movement of the storm intensifies wave development due to the fetch stretching. Waves observed at a given distance $\tilde{X}$ from the rear boundary, have an extended effective fetch $\tilde{X}+\tilde{L}_{cr}$. Thus, waves must be more developed as compared to a stationary storm.

In the context of TC studies, the case for which storm translation velocity is opposite to the wind ($V<0$) must also be considered. To simulate such conditions, the integration constant C in (A15) must be fixed at $C=0$ (in order to satisfy the boundary condition $\alpha \to \infty$ at $\tilde{X}=0$). Then solution reads

$$\alpha^{1/q}\left[1-(1+q)^{-1}\alpha/\alpha_T\right]=c_\alpha^{1/q}\tilde{X}. \tag{A20}$$

Since $\alpha_T<0$, the effective fetch $\tilde{X}_{ef}=\tilde{X}/\left[1-(1+q)^{-1}\alpha/\alpha_T\right]$ is reduced, and thus wind waves at a given distance $\tilde{X}$ from the storm boundary are undeveloped as compared to the stationary storm, Figure A1.

Acknowledgments
Funding by Russian Science Foundation under grant 15-17-20020 and ESA SMOS-Storm and ESA-GasFlux projects are gratefully acknowledged. We are grateful to Sergei Badulin for numerous fruitful discussions on the subject of this work. We thank two anonymous referees who made very helpful comments and suggestions leading to improvement of this paper. The data used in this paper are available at: http://podaac.jpl.nasa.gov/(Jason-1 data); http://www.nodc.noaa.gov/(Jason-2 data); https://earth.esa.int/(CryoSat-2 data); http://www.aviso.altimetry.fr/(SARAL/AltiKa data); http://www.class.ncdc.noaa.gov/(GOES-12 data); http://www.cr.chiba-u.jp/(MTSAT-2 data); http://www.usno.navy.mil/NOOC/nmfc-ph/RSS/jtwc/best_tracks/(TC tracks for western North Pacific); http://www.aoml.noaa.gov/hrd/hurdat/Data_Storm.html (TC tracks for Atlantic).

References

Ardhuin, F., B. Chapron, and F. Collard (2009), Observation of swell dissipation across oceans, *Geophys. Res. Lett.*, *36*, L06607, doi:10.1029/2008GL037030.

Babanin, A. N., and Y. P. Soloviev (1998), Variability of directional spectra of wind-generated waves, studied by means of wave staff arrays, *Mar. Freshwater Res.*, *49*, 89–101, doi:10.1071/MF96126.

Badulin, S. I., A. V. Babanin, V. E. Zakharov, and D. Resio (2007), Weakly turbulent laws of wind-wave growth, *J. Fluid Mech.*, *591*, 339–378, doi:10.1017/S0022112007008282.

Balaguru, K., P. Chang, R. Saravanan, L. R. Leung, Z. Xu, M. Li, and J.-S. Hsieh (2012), Ocean barrier layers' effect on tropical cyclone intensification, *Proc. Natl. Acad. Sci. U. S. A.*, *109*(36), 14,343–14,347, doi:10.1073/pnas.1201364109.

Barruol, G., D. Reymond, F. R. Fontaine, O. Hyvernaud, V. Maurer, and K. Maamaatuaiahutapu (2006), Characterizing swells in the southern Pacific from seismic and infrasonic noise analyses, *Geophys. J. Int.*, *164*, 516–542, doi:10.1111/j.1365-246X.2006.02871.x.

Bowyer, P. J., and A. W. MacAfee (2005), The theory of trapped-fetch waves with tropical cyclones—An operational perspective, *Weather Forecasting*, *20*, 229–244, doi:10.1175/WAF849.1.

Cline, I. M. (1920), Relation of changes in storm tides on the coast of the Gulf of Mexico to the center and movement of hurricanes, *Mon. Weather Rev.*, *48*, 127–146, doi:10.1175/1520-0493(1920)48<127:ROCIST>2.0.CO;2.

Collard, F., F. Ardhuin, and B. Chapron (2009), Monitoring and analysis of ocean swell fields from space: New methods for routine observations, *J. Geophys. Res.*, *114*, C07023, doi:10.1029/2008JC005215.

Delpey, M. T., F. Ardhuin, F. Collard, and B. Chapron (2010), Space-time structure of long ocean swell fields, *J. Geophys. Res.*, *115*, C12037, doi:10.1029/2009JC005885.

Dysthe, K. B., and A. Harbitz (1987), Big waves from polar lows?, *Tellus, Ser. A*, *39*, 500–508, doi:10.1111/j.1600-0870.1987.tb00324.x.

Franklin, J. L., M. L. Black, and K. Valde (2003), GPS dropwindsonde wind profiles in hurricanes and their operational implications, *Weather Forecasting*, *18*, 32–44, doi:10.1175/1520-0434(2003)018 < 0032:GDWPIH>2.0.CO;2.

Gagnaire-Renou, E., M. Benoit, and S. I. Badulin (2011), On weakly turbulent scaling of wind sea in simulations of fetch-limited growth, *J. Fluid Mech.*, *669*, 178–213, doi:10.1017/S0022112010004921.

Grodsky, S. A., N. Reul, G. Lagerloef, G. Reverdin, J. A. Carton, B. Chapron, Y. Quilfen, V. N. Kudryavtsev, and H.-Y. Kao (2012), Haline hurricane wake in the Amazon/Orinoco plume: AQUARIUS/SACD and SMOS observation, *Geophys. Res. Lett.*, *39*, L20603, doi:10.1029/2012GL053335.

Hanafin, J. A., et al. (2012), Phenomenal sea states and swell from a North Atlantic storm in February 2011: A comprehensive analysis, *Bull. Am. Meteorol. Soc.*, *93*, 1825–1832, doi:10.1175/BAMS-D-11-00128.1.

Hasselmann, K., D. B. Ross, P. Müller, and W. Sell (1976), A parametric wave prediction model, *J. Phys. Oceanogr.*, *6*, 200–228, doi:10.1175/1520-0485(1976)006 < 0200:APWPM>2.0.CO;2.

Holland, G. J. (1980), An analytical model of the wind and pressure profiles in hurricanes, *Mon. Weather Rev.*, *108*, 1212–1218, doi:10.1175/1520-0493(1980)108 < 1212:AAMOTW>2.0.CO;2.

Holt, B., and F. I. Gonzalez (1986), SIR-B observations of dominant ocean waves near Hurricane Josephine, *J. Geophys. Res.*, *91*(C7), 8595–8598, doi:10.1029/JC091iC07p08595.

Holt, B., A. K. Liu, D. W. Wang, A. Gnanadesikan, and H. S. Chen (1998), Tracking storm-generated waves in the northeast Pacific Ocean with ERS-1 synthetic aperture radar imagery and buoys, *J. Geophys. Res.*, *103*(C4), 7917–7929, doi:10.1029/97JC02567.

Holthuijsen, L. H., M. D. Powell, and J. D. Pietrzak (2012), Wind and waves in extreme hurricanes, *J. Geophys. Res.*, *117*, C09003, doi:10.1029/2012JC007983.

Hu, K., and Q. Chen (2011), Directional spectra of hurricane-generated waves in the Gulf of Mexico, *Geophys. Res. Lett.*, *38*, L19608, doi:10.1029/2011GL049145.

Husson, R., F. Ardhuin, F. Collard, B. Chapron, and A. Balanche (2012), Revealing forerunners on Envisat's wave mode ASAR using the Global Seismic Network, *Geophys. Res. Lett.*, *39*, L15609, doi:10.1029/2012GL052334.

King, D. B., and O. H. Shemdin (1978), Radar observations of hurricane wave directions, in *Proceedings of 16th International Conference on Coastal Engineering*, pp. 209–226, Am. Soc. of Civ. Eng., Hamburg, Germany.

Kitaigorodskii, S. A. (1962), Applications of the theory of similarity to the analysis of wind-generated water waves as a stochastic process, *Bull. Acad. Sci. USSR Geophys. Ser.*, *1*, 105–117.

Knaff, J. A., M. DeMaria, C. R. Sampson, J. E. Peak, J. Cummings, and W. H. Schubert (2013), Upper oceanic energy response to tropical cyclone passage, *J. Clim.*, *26*, 2631–2650, doi:10.1175/JCLI-D-12-00038.1.

MacAfee, A. W., and P. J. Bowyer (2005), The modeling of trapped-fetch waves with tropical cyclones—A desktop operational model, *Weather Forecasting*, *20*, 245–263, doi:10.1175/WAF850.1.

McPhaden, M. J., G. R. Foltz, T. Lee, V. S. N. Murty, M. Ravichandran, G. A. Vecchi, and L. Yu (2009), Ocean-atmosphere interactions during cyclone Nargis, *Eos Trans. AGU*, *90*(7), 53–54, doi:10.1029/eost2009EO07.

Moon, I.-J., I. Ginis, T. Hara, H. L. Tolman, C. W. Wright, and E. J. Walsh (2003), Numerical simulation of sea surface directional wave spectra under hurricane wind forcing, *J. Phys. Oceanogr.*, *33*, 1680–1706, doi:10.1175/2410.1.

Moon, I.-J., I. Ginis, and T. Hara (2008), Impact of the reduced drag coefficient on ocean wave modeling under hurricane conditions, *Mon. Weather Rev.*, *136*, 1217–1223, doi:10.1175/2007MWR2131.1.

Ochi, M. K. (1993), On hurricane-generated seas, in *Proceedings of the Second International Symposium on Ocean Wave Measurement and Analysis*, pp. 374–387, Am. Soc. of Civ. Eng., New Orleans, La.

Quilfen, Y., J. Tournadre, and B. Chapron (2006), Altimeter dual-frequency observations of surface winds, waves, and rain rate in tropical cyclone Isabel, *J. Geophys. Res.*, *111*, C01004, doi:10.1029/2005JC003068.

Quilfen, Y., B. Chapron, and J. Tournadre (2010), Satellite microwave surface observations in tropical cyclones, *Mon. Weather Rev.*, *138*, 421–437, doi:10.1175/2009MWR3040.1.

Quilfen, Y., D. Vandemark, B. Chapron, H. Feng, and J. Sienkiewicz (2011), Estimating gale to hurricane force winds using the satellite altimeter, *J. Atmos. Oceanic Technol.*, *28*, 453–458, doi:10.1175/JTECH-D-10-05000.1.

Raizer, V. (2007), Macroscopic foam–spray models for ocean microwave radiometry, *IEEE Trans. Geosci. Remote Sens.*, *45*(10), 3138–3144, doi:10.1109/TGRS.2007.895981.

Reul, N., and B. Chapron (2003), A model of sea-foam thickness distribution for passive microwave remote sensing applications, *J. Geophys. Res.*, *108*(C10), 3321, doi:10.1029/2003JC001887.

Reul, N., J. Tenerelli, B. Chapron, D. Vandemark, Y. Quilfen, and Y. Kerr (2012), SMOS satellite L-band radiometer: A new capability for ocean surface remote sensing in hurricanes, *J. Geophys. Res.*, *117*, C02006, doi:10.1029/2011JC007474.

Reul, N., Y. Quilfen, B. Chapron, S. Fournier, V. Kudryavtsev, and R. Sabia (2014), Multisensor observations of the Amazon-Orinoco river plume interactions with hurricanes, *J. Geophys. Res. Oceans*, *119*, 8271–8295, doi:10.1002/2014JC010107.

Ruf, C., A. Lyons, M. Unwin, J. Dickinson, R. Rose, D. Rose, and M. Vincent (2013), CYGNSS: Enabling the future of hurricane prediction, *IEEE Geosci. Remote Sens. Mag.*, *1*(2), 52–67, doi:10.1109/MGRS.2013.2260911.

Smirnova, J. E., P. A. Golubkin, L. P. Bobylev, E. V. Zabolotskikh, and B. Chapron (2015), Polar low climatology over the Nordic and Barents seas based on satellite passive microwave data, *Geophys. Res. Lett.*, *42*, 5603–5609, doi:10.1002/2015GL063865.

Tannehill, I. R. (1936), Sea swells in relation to movement and intensity of tropical storms, *Mon. Weather Rev.*, *64*, 231–238, doi:10.1175/1520-0493(1936)64 < 231b:SSIRTM>2.0.CO;2.

Toba, Y. (1972), Local balance in the air-sea boundary processes: I. On the growth process of wind waves, *J. Oceanogr. Soc. Jpn.*, *28*, 109–120, doi:10.1007/BF02109772.

Tolman, H. L. (2009), User manual and system documentation of WAVEWATCH III version 3.14, *Tech. Note 276*, 194 pp., NOAA/NWS/NCEP/MMAB, Camp Springs, Md.

Uhlhorn, E. W., and P. G. Black (2003), Verification of remotely sensed sea surface winds in hurricanes, *J. Atmos. Oceanic Technol.*, *20*, 99–116, doi:10.1175/1520-0426(2003)020<0099:VORSSS>2.0.CO;2.

Young, I. R. (1988a), A parametric hurricane wave prediction model, *J. Waterw. Port Coastal Ocean Eng.*, *114*(5), 637–652, doi:10.1061/(ASCE)0733-950X(1988)114:5(637).

Young, I. R. (1988b), A shallow water spectral wave model, *J. Geophys. Res.*, *93*(C5), 5113–5129, doi:10.1029/JC093iC05p05113.

Young, I. R. (1993), An estimate of the Geosat altimeter wind speed algorithm at high wind speeds, *J. Geophys. Res.*, *98*(C11), 20,275–20,285, doi:10.1029/93JC02117.

Young, I. R. (1998), Observations of the spectra of hurricane generated waves, *Ocean Eng.*, *25*(4), 261–276, doi:10.1016/S0029-8018(97)00011-5.

Young, I. R. (2003), A review of the sea state generated by hurricanes, *Mar. Struct.*, *16*, 201–218, doi:10.1016/S0951-8339(02)00054-0.

Young, I. R., and J. Vinoth (2013), An "extended fetch" model for the spatial distribution of tropical cyclone wind-waves as observed by altimeter, *Ocean Eng.*, *70*, 14–24, doi:10.1016/j.oceaneng.2013.05.015.

Young, I. R., A. V. Babanin, and S. Zieger (2013), The decay rate of ocean swell observed by altimeter, *J. Phys. Oceanogr.*, *43*(11), 2322–2333, doi:10.1175/JPO-D-13-083.1.

Zabolotskikh, E. V., L. M. Mitnik, and B. Chapron (2013), New approach for severe marine weather study using satellite passive microwave sensing, *Geophys. Res. Lett.*, *40*, 3347–3350, doi:10.1002/grl.50664.

Zabolotskikh, E. V., L. M. Mitnik, N. Reul, and B. Chapron (2015), New possibilities for geophysical parameter retrievals opened by GCOM-W1 AMSR2, *IEEE J. Selec. Top. Appl. Earth Obs. Remote Sens.*, doi:10.1109/JSTARS.2015.2416514, in press.

Zakharov, V. E. (2005), Theoretical interpretation of fetch limited wind-driven sea observations, *Nonlinear Processes Geophys.*, *12*, 1011–1020, doi:10.5194/npg-12-1011-2005.

Zakharov, V. E., and M. M. Zaslavsky (1983), Dependence of wave parameters on the wind velocity, duration of its action and fetch in the weak-turbulence theory of water waves, *Izv. Atmos. Oceanic Phys.*, *19*(4), 300–306.

Zakharov, V. E., S. I. Badulin, P. A. Hwang, and G. Caulliez (2015), Universality of sea wave growth and its physical roots, *J. Fluid Mech.*, *780*, 503–535, doi:10.1017/jfm.2015.468.